TITLE

Large haploblocks underlie rapid adaptation in an invasive weed

AUTHORS

Paul Battlay[1], Jonathan Wilson[1], Vanessa C. Bieker[2], Chris Lee[1], Diana Prapas[1], Bent Petersen[3,4], Sam Craig[1], Lotte van Boheemen[1], Romain Scalone[5,6], Nissanka P. de Silva[1], Amit Sharma[7], Bojan Konstantinović[8], Kristin A. Nurkowski[1,9], Loren Rieseberg[9], Tim Connallon[1], Michael D. Martin[2], Kathryn A. Hodgins[1]*

These authors contributed equally: Paul Battlay, Jonathan Wilson

These authors jointly supervised this work: Kathryn A. Hodgins, Michael D. Martin

[1] School of Biological Sciences, Monash University, Melbourne, Victoria, Australia

[2] Department of Natural History, NTNU University Museum, Norwegian University of Science and Technology (NTNU), Trondheim, Norway

[3] Center for Evolutionary Hologenomics, GLOBE Institute, University of Copenhagen, Denmark

[4] Centre of Excellence for Omics-Driven Computational Biodiscovery (COMBio), AIMST University, 08100 Kedah, Malaysia

[5] Department of Crop Production Ecology, Uppsala Ecology Center, Swedish University of Agricultural Sciences, Uppsala, Sweden.

[6] Department of Grapevine Breeding, Hochschule Geisenheim University, Geisenheim, Germany.

[7] Cell, Molecular Biology and Genomics Group, Department of Biology, Norwegian University of Science and Technology (NTNU), Trondheim, Norway

[8] Department of Environmental and Plant Protection, University of Novi Sad, Novi Sad, Serbia

[9] Department of Botany and Biodiversity Research Centre, University of British Columbia, Vancouver, Canada

ABSTRACT

Adaptation is the central feature and leading explanation for the evolutionary diversification of life. Adaptation is also notoriously difficult to study in nature, owing to its complexity and logistically prohibitive timescale. We leverage extensive contemporary and historical collections of *Ambrosia artemisiifolia*—an aggressively invasive weed and primary cause of pollen-induced hayfever—to track the phenotypic and genetic causes of recent local adaptation across its native and invasive ranges in North America and Europe, respectively. Large haploblocks—indicative of chromosomal inversions—contain a disproportionate share of genomic regions conferring parallel adaptation to local climates between ranges (18%), are associated with rapidly adapting traits, and exhibit dramatic frequency shifts over space and time. These results highlight the importance of large-effect standing variants in rapid adaptation, which have been critical to *A. artemisiifolia*'s global spread across vast climatic gradients.

INTRODUCTION

Adaptation can be rapid, yet changes in the traits and genes that underlie adaptation are difficult to observe in real time because speed is relative: that which is fast in evolutionary terms is slow from the human perspective. Thus, while we know that adaptation is central to evolutionary diversification, species persistence, and invasiveness, the genetic and phenotypic dynamics of adaptation are difficult to document outside of the laboratory.

Invasive species are powerful systems for characterizing adaptation in nature, owing to several features that make them unique. In particular, biological invasions coincide with exceptionally rapid evolution[1–3], observable over human lifespans, as invasive populations can encounter drastically different environmental conditions from those of their source populations. Many invasions are, moreover, documented in large, geo-referenced herbarium collections, which can be phenotyped and sequenced to identify and track adaptive evolutionary changes through time—feats that are rarely achieved in natural populations. Invasive species frequently inhabit broad and climatically diverse ranges, which favours the evolution of adaptations to local environmental conditions[2,3], along with evolved tolerance of environmental extremes, which may be conducive to invasiveness[4]. Because they often occupy geographically broad native and invasive ranges, invasive species allow for tests of the predictability of evolution—a major puzzle in biology—as local adaptation across native and invasive ranges may favour either parallel or unique genetic solutions to shared environmental challenges. However, despite the promise of historical records and other features of invasive species that make them tractable systems for capturing adaptation in action, this treasure trove of data has not been fully utilized to elucidate the genetic basis of local adaptation during recent range expansions.

Ambrosia artemisiifolia, an annual weed native to North America, has mounted successful invasions on all continents except Antarctica[5]. The species thrives in disturbed habitats and has experienced extensive range shifts, historically documented in pollen records and herbarium collections. It also produces highly allergenic pollen, which is the chief cause of seasonal allergic rhinitis and asthma in the United States[6]. In Europe alone, approximately 13.5 million people suffer from *Ambrosia*-induced allergies, costing ~7.4 billion euros annually[7]. Continued invasion and climate change are predicted to more than double sensitization to *Ambrosia* pollen[8], further magnifying the health burden of this pest. Pollen monitoring has demonstrated that climate change has already significantly lengthened the ragweed pollen season, particularly at high latitudes[9]. Consequently, there is considerable incentive to understand the factors that

contribute to *Ambrosia* pollen production, including the species' invasive spread, the timing of pollen production, plant size, and fecundity.

Ambrosia artemisiifolia populations are characterized by strong local adaptation and high gene flow between populations[10,11]. In Europe, invasive populations have been established through multiple genetically diverse introductions from North America over the last ~160 years[11–13]. Remarkably, latitudinal clines observed for multiple traits in the native range, including flowering time and size, have re-evolved in Europe and Australia[14], suggesting rapid local adaptation following invasion. Moreover, this trait-level parallelism is echoed in signals of parallelism at the genetic level[10].

As biological invasions continue to increase worldwide[15] and the effects of anthropogenic climate change intensify, understanding the genetic architecture of adaptation to sudden environmental shifts—a classical question in evolutionary research—becomes ever more important. While long-standing theory suggests that evolution in response to incremental environmental change should proceed through mutations of infinitesimally small[16] or moderate[17] effect, large-effect mutations are predicted to be useful in bridging extreme, sudden environmental shifts[18]. Moreover, alleles of large effect will, in cases of local adaptation, be better able to persist in the face of the swamping effects of gene flow[19]. Large-effect mutations are also more likely to produce patterns of evolutionary repeatability, or genetic parallelism, between species' ranges[20], particularly if adaptive responses make use of standing genetic variation (as would be expected during a bout of rapid adaptation), rather than *de novo* mutations[21]. These features of large-effect mutations may, however, be achieved by groups of mutations in tight genetic linkage[19], including mutations captured by chromosomal inversions[22]. There is substantial empirical evidence for the involvement of inversions in local adaptation[23]. For example, *Drosophila melanogaster*'s *In(3R)Payne* inversion shows parallel environmental associations across multiple continents[24], and several plant inversions have been identified as contributing to local adaptation and ecotype divergence[25,26]. Theory also predicts that inversions can drive range expansions[27], though their actual contributions to biological invasions are not well-understood.

Here we develop a new, high quality and near chromosome-level reference assembly, and examine genome-wide variation in over 600 modern and historic *A. artemisiifolia* samples from throughout North America and Europe[11]. Using this data of unparalleled spatial and temporal

resolution, we first identified regions of the genome experiencing climate-mediated selection in the native North American and introduced European ranges leveraging landscape genomic approaches and genome-wide association studies of adapting traits such as flowering time. Second, motivated by evidence that European and North American populations show similar trait clines with respect to climate[14], we examined the extent of between-range parallelism at the genetic level. Although adapting traits such as flowering time and size are polygenic, we expected to see substantial levels of parallelism if large and moderate effect standing variants were contributing to adaptive divergence. Third, we determined if these same regions show temporal signatures of selection in Europe, which would be expected if some invading populations were initially maladapted to their local climates. We coupled this temporal genomic analysis with a temporal analysis of phenological trait changes in European herbarium samples to further support our findings of genomic signatures of selection on flower time genes. Finally, we identified haplotype blocks with multiple features consistent with inversions, in genomic regions enriched for signatures of parallel adaptation. To determine if these putative structural variants were contributing to rapid local adaptation in Europe, we assessed spatial and temporal changes in their frequency as well as their associations with adapting traits.

RESULTS

Reference genome assembly

We assembled a new, near chromosome-level *Ambrosia artemisiifolia* reference genome from a heterozygous, diploid individual collected from Novi Sad, Serbia. After purging uncollapsed heterozygosity[28] and scaffolding with HiRise[29] our final assembly consisted of 395 scaffolds, with an L_{90} of 20 (*A. artemisiifolia* has 18 chromosomes[30]) and a genome size of 1.2Gb (flow cytometry estimates of genome size range from 1.13-1.16Gb[31,32]). A total of 253 complete Benchmarking Universal Single-Copy Orthologs (BUSCO[33]) genes (99.2%; 138 single copy [54.1%]; 115 duplicated [45.1%]), no fragmented BUSCO genes and two missing BUSCO genes (0.8%; table S1) were identified. The high numbers of duplicated BUSCO genes likely reflect the whole genome duplications experienced in the Asteraceae, including a recent one shared by *Helianthus* (sunflower) species at the base of the tribe[34,35]. This species also retained a large number of duplicated BUSCO genes[35]. A large fraction of the genome consisted of repetitive sequence (67%; table S2). Retroelements were the largest class (39.5%), with LTRs, particularly Gypsy (7.87 %) and Copia (18.98 %), the most prevalent retroelements. MAKER [36] identified 29,849 gene models with strong protein or transcript support, with average coding lengths of 1.09kb, and 7.18 exons per gene (table S3; fig S1).

Genome-wide association studies

Genome-wide association studies (GWAS) using 121 modern samples across North American (n = 43) and European (n = 78; table S4) ranges identified significant associations with 13 of 30 phenotypes, many of which are putatively adaptive, previously measured by van Boheemen, Atwater and Hodgins[14] (fig. S2; table S5). Six phenotypes yielded associations within predicted genes, including an association between flowering time phenotypes and a nonsynonymous SNP in the *A. artemisiifolia* homologue of *A. thaliana* flowering-time pathway gene *early flowering 3* (*ELF3*[37]), an "evolutionary hotspot" for parallel flowering time adaptation in *A. thaliana*, barley and rice[38] (table S5; fig. 1A;B). Candidate SNPs in *ELF3* are restricted to high-latitude populations in both ranges, where they occur at moderate to high frequencies (fig. 1C). While the latitudes of these populations are greater in Europe than North America, the climatic conditions are similar (fig. S3), indicative of local climate adaptation in parallel between ranges.

Environmental-allele associations

To identify genome-wide spatial signatures of local adaptation in North American and European ranges, we performed genome scans for population allele frequencies among *A. artemisiifolia*

158 modern samples that were both highly divergent between populations (BayPass XtX)[39], and
159 correlated with environmental variables (latitude, longitude and 19 WorldClim temperature and
160 precipitation variables; table S6)[40]. Statistics were analyzed in 10kb windows using the
161 Weighted-Z Analysis (WZA)[41]. In North America (143 samples; 43 populations), 1,480 (84.0%)
162 of the 1,762 outlier windows for genomic divergence (XtX) were also outlier windows for at least
163 one environmental variable (XtX-EAA), while in Europe (141 samples; 31 populations), only 908
164 (51.7%) of the 1,755 XtX outlier windows overlapped environmental variable outlier windows.
165 Signatures of local adaptation were much stronger in North America than Europe, with the North
166 American range showing more extreme XtX values (fig. 1C), as well as more XtX-EAA windows
167 (table S6; fig. 1C). This suggests that North America exhibits greater population differentiation,
168 and a stronger relationship between population differentiation and the environment than Europe,
169 which is consistent with the expectation that samples from the native range will be better-
170 adapted to their environment than those from the recently-invaded European range.
171
172 Previous studies in *A. artemisiifolia* have identified signatures of repeatability between native
173 and invasive ranges at phenotypic and genetic levels[10,14]. We observed congruent patterns in
174 our data: among North American and European XtX-EAA outlier windows, 173 showed parallel
175 associations with the same environmental variable between ranges (significantly more than
176 would be expected by chance; hypergeometric $p = 4.39\times10^{-63}$; fig. 1C), with 19% of climate
177 adaptation candidates in Europe also candidates in North America. To account for the possibility
178 that the number of parallel windows is inflated by extended linkage disequilibrium between
179 windows (and hence represents a smaller number of loci), we combined consecutive windows,
180 and windows in haploblock regions, into single windows and repeated the analysis, in which the
181 parallelism remained highly significant (hypergeometric $p = 1.08\times10^{-63}$). Consequently, many of
182 the same regions of the genome are involved in climate adaptation in both ranges.
183
184 In addition to *ELF3*, parallel XtX-EAA outlier windows included four windows within two
185 previously identified flowering-onset QTL[42]. North American, European and parallel XtX-EAA
186 outlier windows included 17, ten, and three flowering-time pathway genes, respectively,
187 however this only represented a significant enrichment (Fisher's exact test $p < 0.05$) in North
188 America (table S7). Gene ontology terms enriched in parallel XtX-EAA windows included "iron
189 ion binding" and "heme binding" (terms relating to cytochrome P450 genes), as well as
190 "gibberellin biosynthetic process" (table S8). Some cytochrome P450 genes are involved in
191 detoxification of xenobiotic compounds and the synthesis of defense compounds, while others

192 play key developmental roles[43], including contributing to the biosynthesis of gibberellin, a
193 hormone that regulates a range of developmental events, including flowering[44].

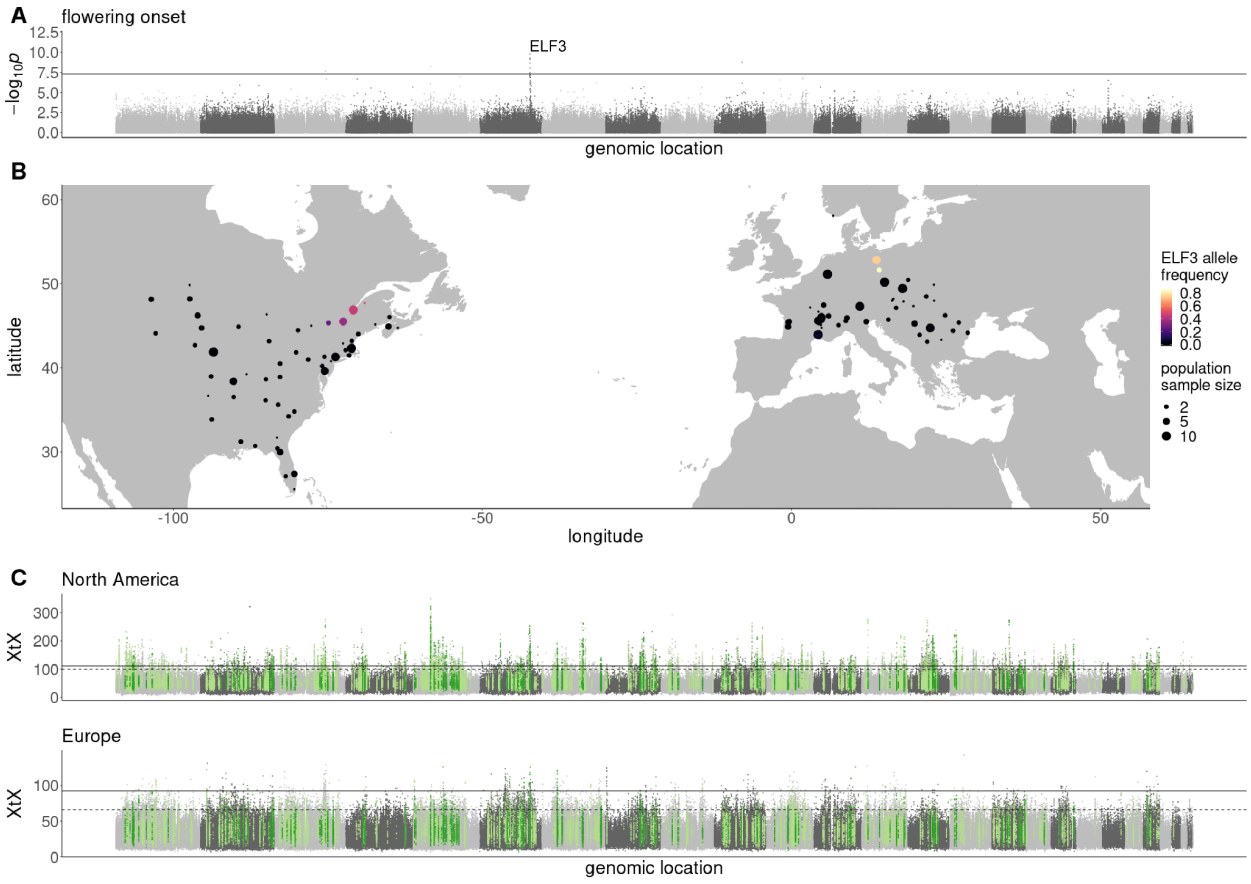

Figure 1. Signatures of climate adaptation in *Ambrosia artemisiifolia*. A. GWAS results ($-\log_{10}p$ against genomic location) for flowering onset (solid line indicates a Bonferroni-corrected p-value of 0.05). **B.** Distribution of a strongly-associated nonsynonymous SNP in ELF3 among modern *A. artemisiifolia* populations used in this study. **C.** Genome-wide XtX scans between sampling locations within each range separately. Solid lines indicate Bonferroni-corrected significance derived from XtX *p*-values; dashed lines indicate the top 1% of genome-wide XtX values. Green highlights represent the top 5% of 10kb WZA windows for each scan that are also among the top 5% of EAA WZA windows for at least one environmental variable, with dark green indicating windows shared between North America and Europe.

Temporal phenotypic analysis

To further identify the features of recent adaptation in *A. artemisiifolia*, we leveraged herbarium samples, collected from as early as 1830, for phenotypic and genomic analyses. A trait-based analysis of 985 digitized herbarium images (fig. S4) identified a significant shift in the probability of flowering and fruiting over time in Europe, but this change depended on the latitude or the day of the year the sample was collected (fig. S5; table S9). For the trait presence of a mature male inflorescence, we identified a significant interaction between collection year and latitude ($F_{1,886}$ = 7.89, p < 0.01) where in northern populations, more recently collected plants were more likely to be flowering than older historic specimens. For this trait, collection day also significantly interacted with collection year and more recently collected plants were more likely to be flowering later in the year and less likely to be flowering earlier in the year. Similar patterns were identified with the presence of fruit, as older samples were less likely to produce fruit later in the season compared to recent samples (day-by-year interaction $F_{1,886}$ = 32.33, p < 0.001; fig. S5; table S10). This substantial spatio-temporal change in phenology is consistent with experimental common gardens that show that earlier flowering has evolved in northern populations and later flowering in southern populations following the invasion of Europe[14]. Further, this shift in both flowering and fruit set over time supports the hypothesis that an initial mismatch between the local environment and the genotypes present impacted the reproductive output of *A. artemisiifolia* during the early stages of colonization, particularly in northern Europe.

Temporal genomic signatures of selective sweeps

Genome resequencing of *A. artemisiifolia* herbarium samples[11] allowed comparisons between historic and modern populations. We grouped historic samples based on their age and proximity to a modern population sample, resulting in five North American and seven European historic-modern population pairs (table S11), which were scanned for signatures of local selective sweeps by identifying windows with extreme shifts in allele frequency and extreme reductions in diversity over time. We found far more evidence for recent sweeps in Europe (494 unique windows) than in North America (113 unique windows; fig. S6 c.f. S7; table S11), consistent with the expectation that a haphazardly-introduced invader will frequently be maladapted, initially, and undergo rapid adaptation to local environmental conditions following its introduction. The most dramatic selective sweep signatures were observed in Berlin and two French populations in a ~16Mb region on scaffold 448 (fig. 2A; fig. S7), which accounts for 312 (63%) of the European sweep windows. In Berlin, sweep windows were also observed containing and surrounding the flowering onset GWAS peak that includes *ELF3*. In comparisons of spatial and

237 temporal signatures of selection, two and nine sweep windows were also XtX-EAA outliers in
238 North America and Europe respectively. All such windows in Europe were in the scaffold 448 or
239 *ELF3* regions. To further investigate the temporal shift associated with *ELF3*, we focused on the
240 nonsynonymous *ELF3* variant across all samples within a 200km radius of Berlin (15 historic
241 and eleven modern samples). The frequency of the variant increased from 4.9% to 73.9%
242 between historic and modern samples, an allele frequency shift greater than 10,000 putatively
243 neutral loci sampled from the same geographic region (fig. 2C); similar shifts were not observed
244 in North American samples within a 200km radius of Quebec City (ten historic and eleven
245 modern), where the *ELF3* allele is at comparably high frequencies (fig. S8).

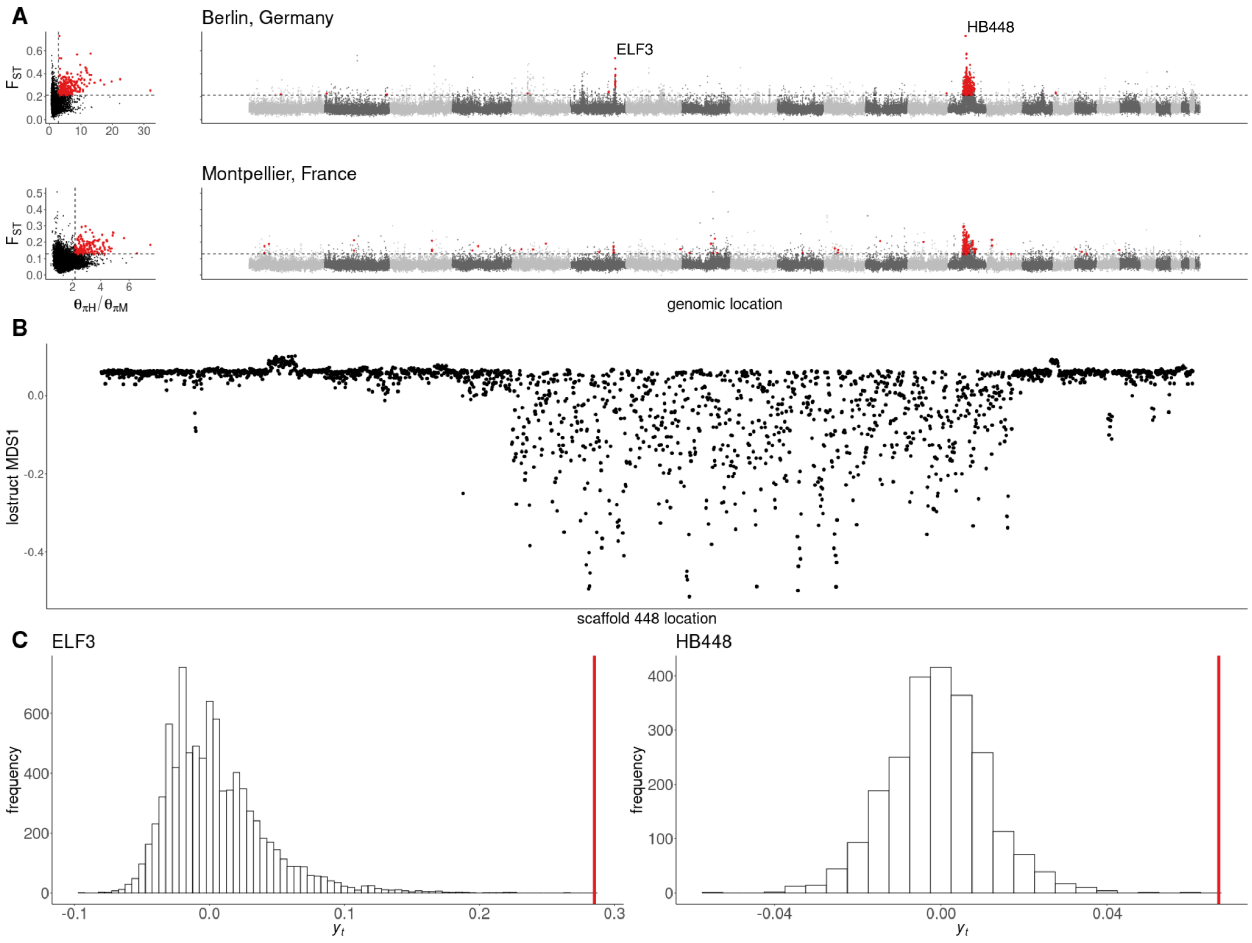

Figure 2. Temporal signatures of selective sweeps in Europe. A. Distributions of F_{ST} between historic and modern samples and the ratio of historic to modern nucleotide diversity ($\theta_{\pi H}/\theta_{\pi M}$) from Berlin and Montpellier, and F_{ST} against genomic location. Red points indicate putative selective sweep windows, which are in the top one percent of per-window F_{ST} and $\theta_{\pi H}/\theta_{\pi M}$ (dashed lines). **B.** Strong evidence for a selective sweep on scaffold 448 in European populations corresponds with local divergent population structure (MDS1), indicating the presence of a haploblock (putative chromosomal inversion) in this region. **C.** Distributions of values of a standardized measure of allele frequency change, y_t (calculated according to equation 1; histograms) for shifts between historic and modern populations across putatively neutral SNPs. y_t for scaffold 2 position 56,025,662, a nonsynonymous SNP in *ELF3* (red line), against a distribution of y_t values from 10,000 putatively neutral SNPs from samples within 200km of Berlin (left) and y_t calculated from the haplotype frequency of HB448 (red line), against a distribution of y_t values from 7,394 putatively neutral SNPs from across the European range (right).

Haploblock identification

Chromosomal inversions have previously been identified as driving local adaptation of ecotypes of *Helianthus* species[26]. We used a similar approach to identify genomic signatures of putative inversions (haploblocks) contributing to local adaptation in *A. artemisiifolia*. Briefly, we identified genomic regions in which population structure was divergent and fell into three clusters, putatively representing the heterozygous and two homozygous genotypic classes of an inversion. Further, we looked for pronounced shifts in population structure (indicating inversion breakpoints), elevated local heterozygosity in the heterozygous cluster, and increased linkage disequilibrium across the region (fig. S9). Finally, we examined mapping populations of *A. artemisiifolia*[42] for evidence of map-specific reductions in recombination across haploblock regions (i.e., suppressed recombination in haploblock regions in some maps but not others; fig. S10). This would be the pattern expected when recombination is suppressed by inversions in heterozygotes but not homozygotes, as opposed to the haploblocks being caused by global reductions in recombination in those regions. All haploblocks showed evidence of suppressed recombination in some maps but not others, with the exception of HB31 which showed suppressed recombination in all maps.

Focussing our analysis on regions showing signatures of adaptation, we identified seven haploblocks with the above genomic signatures of chromosomal inversions overlapping the 173 WZA windows that were parallel outliers for both XtX and at least one climate variable: HB2 (2.4Mb), HB5 (5.2Mb), HB21 (13.4Mb), HB27a (4.1Mb), HB27b (5.5Mb), HB31 (6.7Mb) and HB448 (16.1Mb). These haploblocks contained 31 of the 173 windows (17.9%; fig. S11), with one haploblock also corresponding to the European selective sweep region on scaffold 448 (fig. 2A;B). This suggests that these haploblock regions have played a pivotal role in generating parallel signatures of selection observed in *A. artemisiifolia*.

Haploblock frequency changes through space and time

To identify changes in haploblock frequency over time and space, which would be consistent with selection on these putative inversions, we first estimated haploblock genotypes for all historic and modern samples. Within haploblock boundaries identified using modern sample SNP data in Lostruct[45], we performed local PCAs with both historic and modern samples (table S4) and identified genotypes by kmeans clustering (fig. S9). For modern samples, we used generalized linear models to estimate the slopes of the haploblock frequencies as a function of latitude within each range. For those haploblocks that were significantly associated with latitude,

we compared these estimates with the genome-wide distribution of slopes for North America and Europe, based on 10,000 unlinked SNPs that were randomly selected from outside haploblocks and genes. The estimated slopes for haploblocks HB27a, HB27b and HB31 fell into the 5% tail of the distribution for at least one of the ranges (fig. S12). However, this approach did not examine temporal changes nor the combined signatures of selection over space and time. To do so, we ran generalized linear models comparing haplotype frequency with latitude, time (date of specimen in years) and range (North America vs. Europe; fig. 3A; fig. S13; table S12-S17). All of the haploblocks showed significant changes over time, either in their average frequency in one or both ranges, or in their relationship with latitude within each range, a pattern that is consistent with local selection on the haploblocks. All seven haploblocks showed significant associations with time or with latitude in at least one range, indicative of climate adaptation. These patterns were robust to time being coded as discrete (historic vs. modern) or as continuous (by year; table S12). In HB5, HB27b and HB31, we identified significant three-way interactions between latitude, time and range (fig. 3A). The HB27b haplotype frequency was correlated with latitude in modern and historic samples from North America, as well as in modern European samples, consistent with climate-mediated selection. However, historic European populations did not display an association with latitude, which may reflect maladaptation during the initial stages of the European range expansion (fig. 3A; table S15, S17). A significant strengthening of the relationship between latitude and haplotype frequency was also observed in HB5.

To further investigate whether European populations showed evidence of recent local selection on the haploblocks, we tested whether estimates of selection inferred from contemporary spatial data were associated with temporal changes in haploblock frequencies between historical and contemporary European populations. We used spatial variation in contemporary haploblock frequencies to estimate the relative strength of local selection on these haploblocks (see supplementary text S2). We specifically compared estimates of the maximum slope of latitudinal clines for each putative inversion's frequency to simple population-genetic models for clines at equilibrium between local selection and gene flow. In these models, cline slopes are proportional to $\sqrt{s}/\sigma$, where s represents the strength of local selection for a given inversion and σ is the average dispersal distance of individuals in the range[46] (supplementary text S2). While our estimates of selection are, therefore, scaled by the dispersal rate, dispersal should equally affect all inversions within a given range, allowing us to infer the relative strength of spatially varying selection for each putative inversion. We found that estimates of the relative strengths of

local selection across the haploblocks were correlated between the ranges, indicating parallel patterns of local selection along the latitudinal gradient (r = 0.80, p = 0.03). We also found that changes in the haploblock cline slopes between historic and modern time points within Europe were significantly correlated with our estimates of the relative strength of spatially varying selection of the haploblocks across the European range (r = 0.86, p = 0.01 fig. S14). Such a pattern is consistent with a scenario in which historical European populations were not initially locally adapted (haploblock frequencies were initially far from local optima) and where the haploblocks subject to relatively strong local selection exhibited the greatest temporal changes in local frequency over the ensuing century. The same pattern was not observed in the North American native range, whose historic populations are likely to have been consistently closer to the local optima across the timescale of our analysis (r = 0.61, p = 0.15). Cline slopes for latitude were also shallower in historic relative to modern European populations ($t_{6.58}$ = -2.39, p = 0.05; mean absolute slope: historic EU = 0.05; modern EU = 0.15), but not so in North America ($t_{11.9}$ = 0.24, p = 0.81), consistent with initial maladaptation in Europe, followed by adaptation to local climates.

The HB448 haplotype frequency dramatically increased in the European invasive populations over time, consistent with strong range-wide selection in Europe (table S12). The haploblock also showed a significant range effect, with a significantly higher frequency in modern Europe compared to North America (historic and modern) and historic Europe (table S14). Latitudinal clines in frequency were also observed although the clinal patterns were similar over time and between ranges. Signatures of selective sweeps were observed in the HB448 region in multiple European populations (fig. 2A; fig. S10). To further distinguish the effects of drift from those of selection, we compared an empirical null distribution of allele frequency changes over time in Europe using 2,296 SNPs matched for allele frequency (fig. 2C). Only a single locus in this null distribution showed an allele frequency change greater than HB448. We then estimated the strength of selection for the putative inversion under scenarios of positive and balancing selection (see supplementary text S1). With positive selection for the putative inversion, the observed changes in frequency are consistent with a 2.2% difference in fitness (95% CI = {1.6%, 2.8%}) between individuals homozygous for the inversion relative to homozygotes for the alternative haplotype. Scenarios of balancing selection require stronger selection to explain the inversion frequency shift over time (see supplementary text S1). This estimate is smaller than many empirical estimates of selection on individual loci in natural populations[47]. The greater

timespan of our samples facilitated detection of strong signals of selection for loci that would otherwise be missed by the short time periods afforded by most temporal studies.

Biological functions of haploblocks

Several analyses provide evidence for the biological function of these putatively adaptive haploblocks. From genome annotations, we found that haploblocks were collectively enriched for flowering-time pathway genes (Fisher's exact test $p = 0.034$), although individual haploblocks were not significantly enriched (table S18). HB448 was enriched for the "recognition of pollen" gene ontology term, with 28 (17%) of the genome's 167 genes annotated with this term falling within this haploblock (table S19). HB27a was enriched for genes with the "pectate lyase activity" term, including the top BLAST hit for *Amba1* (99.7% identity, *E*-value = 0), which encodes the *A. artemisiifolia* protein responsible for the majority of allergic reactions[48]. A detailed analysis of the HB27a region reveals a cluster of six closely-related pectate lyase genes, which correspond with elevated XtX and XtX-EAA outlier windows in both ranges (fig. S15). HB27b corresponds to a large-effect flowering time and height QTL[42]. HB2 also overlaps the flowering time GWAS candidate *ELF3* (fig. 1A;B), and the nonsynonymous variant which displays strong patterns in GWAS is only observed on one of the haploblock genotype backgrounds. We also identified phenotypic associations with haploblocks by encoding haploblock genotypes into our GWAS pipeline. Significant associations ($p < 0.05$ Bonferroni-corrected for multiple testing across seven haploblocks) were observed for five haploblocks; four haploblocks showed associations with traits related to flowering time (fig. 3B; table S20).

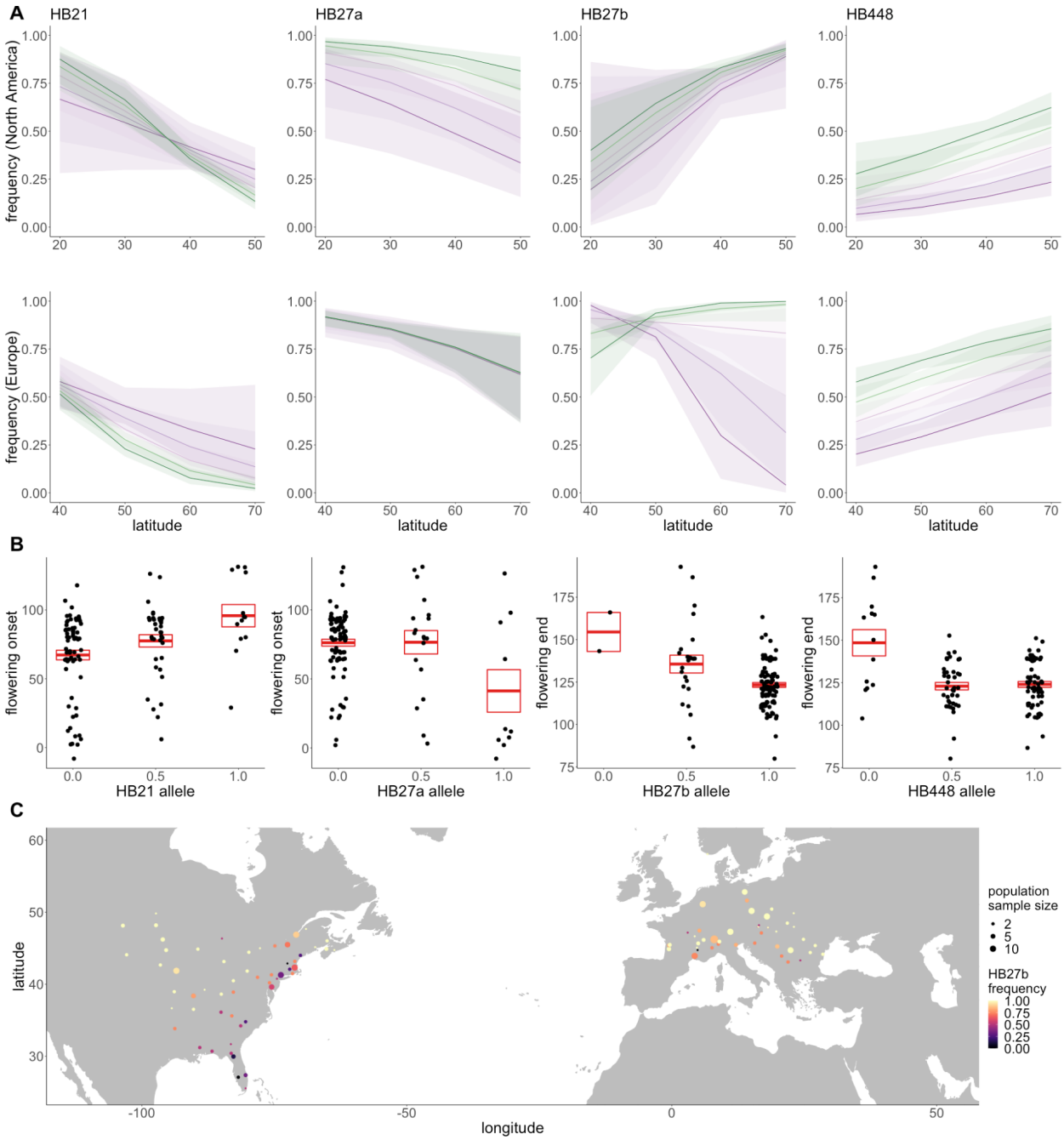

Figure 3. Haploblock distributions and trait associations. A. Logistic regression models with 95% CI ribbons (see table S12-17 for model details) of haploblock frequency (allele 1) against latitude for four haploblocks across five time bins ranging from most historic (purple) to most modern (green). **B.** Examples of significant associations between haploblock alleles and phenotypes (boxes denote mean and SEM). **C.** HB27b allele frequency in modern *A. artemisiifolia* populations.

DISCUSSION

We have described, at an unprecedented temporal and spatial resolution, the evolutionary-genetic changes accompanying a recent and rapid invasion by a noxious pest. Our study system, while unique in many ways, yields results with important general implications for our understanding of the genetic basis of rapid adaptation to environmental change and the pervasiveness of parallel evolution in geographically widespread species.

While invasive species are often envisaged to encounter novel selection pressures as they spread across alien landscapes, they must also readapt to similar environmental variation encountered in their native range, as haphazardly-introduced invaders are unlikely to be well-adapted to local conditions when the invasive populations initially expand across climatic gradients. Much of *Ambrosia artemisiifolia*'s European invasion lies within climatic extremes encountered across its native range (fig. S3). Despite this similarity in climatic variation, the patterns of parallel climate adaptation between native and invasive ranges are striking given the evolutionarily recent introduction of the species into Europe. As *A. artemisiifolia*'s invasion of Europe consisted of multiple introductions over a brief evolutionary time scale, these patterns are likely examples of 'collateral evolution'[49], in which standing genetic variation in *A. artemisiifolia*'s native range has been co-opted for adaptation in and across the European invasive range. Parallel evolution is a hallmark of natural selection and parallel changes at the genetic level point to constraints and biases in the genetic pathways to adaptation that are evolutionarily achievable; when certain paths to adaptation are favored, such as when beneficial variants are already present in the population as standing variants, evolution will repeatedly draw on the same subset of genes to reach the same adaptive endpoints.

From herbarium specimens that were sampled throughout the course of *A. artemisiifolia*'s invasion of Europe, we observed an abrupt change in flowering and fruiting over time. Leveraging whole-genome sequences of herbarium samples across North America and Europe, we were also able to scan populations for temporal genomic signatures of selective sweeps. Although some populations have experienced shifts in ancestry over time in Europe[11], peaks against the genome-wide background provide compelling evidence for rapid local adaptation in European populations, with the strongest genetic signals of rapid change over time corresponding to some of the strongest signatures of local adaptation in our spatial analyses, particularly windows in the region of the *ELF3* gene and HB448. Further, these regions show parallel signals of climate adaptation in North America and are associated with adapting traits

such as flowering onset. These multiple lines of evidence provide strong support that climate mediated selection on phenology was pivotal in shaping the adaptive genetic landscape of *A. artemisiifolia* in Europe.

Large haploblocks (putative inversions) contribute substantially to these genetic signals of parallel adaptation. We propose that these haploblocks maintain cassettes of co-selected genes that effectively segregate as single alleles of large effect[22,27], providing a genetic architecture suited to local adaptation in the face of high gene flow[11,19]. Consistent with this hypothesis, haploblocks are enriched for genes with particular biological functions, display associations with locally-adaptive traits, and carry signals of strong selection in both the native and invasive ranges. The evolution of inversions along environmental gradients has been reported in a range of species[23]. However, by investigating haploblocks in an invasive plant with extensive timestamped collections, we have demonstrated dramatic and adaptive evolutionary change of putative inversions under natural conditions, providing compelling evidence of strong and recent natural selection. These data have also allowed us to estimate selection for these variants, and we have shown that haploblocks with the strongest estimates of clinal selection are driven more rapidly towards their putative equilibria within the invasive range.

An important question during this era of environmental upheaval is the role of adaptation during range expansion and its necessity during colonization. Through our analysis of historic samples, we have shown that *A. artemisiifolia* was present in regions throughout Europe well before many of these adaptive variants became locally common, suggesting the species' extensive phenotypic plasticity may have facilitated its initial expansion. Strong local selection further improved the match between genotypes and local environments, even appearing to affect reproductive output in herbarium specimens. Many of the selected variants we identified are linked to traits that are key factors in the timing, length and severity of the local pollen season (e.g. days to flowering onset, days to the end of pollen production, and biomass). Consequently, local adaptation has played a central role in shaping the allergy season in Europe and will likely continue to be critical as climate change and continued range expansion further amplify the damaging effects of this hazardous weed[50].

METHODS

Genome assembly

Seeds collected from a wild *Ambrosia artemisiifolia* population in Novi Sad, Serbia (lat. 45.25472, lon. 19.91231) were sown in potting soil at a greenhouse facility at the Ringve Botanical Garden, NTNU University Museum (Trondheim. Norway). After 160 days of growth under stable light and watering conditions, young leaf tissue from mature individual plant "NSS02/B" was sampled and flash-frozen in liquid nitrogen. These tissues were then shipped to Dovetail Genomics for high molecular weight DNA extraction and library building.

DNA samples were quantified using Qubit 2.0 Fluorometer (Life Technologies, Carlsbad, CA, USA). The PacBio SMRTbell library (~20kb) for PacBio Sequel was constructed using SMRTbell Express Template Prep Kit 2.0 (PacBio, Menlo Park, CA, USA) using the manufacturer recommended protocol. The library was bound to polymerase using the Sequel II Binding Kit 2.0 (PacBio) and loaded onto PacBio Sequel II). Sequencing was performed on PacBio Sequel II 8M SMRT cells generating 65.9 Gb of data. These PacBio CCS reads were used as an input to Hifiasm[51] with default parameters.

For each Dovetail Omni-C library, chromatin was fixed in place with formaldehyde in the nucleus and then extracted. Fixed chromatin was digested with DNAse I, chromatin ends were repaired and ligated to a biotinylated bridge adapter followed by proximity ligation of adapter containing ends. After proximity ligation, crosslinks were reversed and the DNA purified. Purified DNA was treated to remove biotin that was not internal to ligated fragments. Sequencing libraries were generated using NEBNext Ultra enzymes and Illumina-compatible adapters. Biotin-containing fragments were isolated using streptavidin beads before PCR enrichment of each library. The library was sequenced on an Illumina HiSeqX platform to produce ~30x sequence coverage. Then HiRise used (See read-pair above) MQ>50 reads for scaffolding.

The HiFi assembly yielded a 2.1-Gbp genome, substantially larger than previous genome size estimates of 1.13-1.16Gbp[31,32]. We used GenomeScope 2.0 to estimate the genome size and ploidy using 21mers identified in the reads with Jellyfish 2.3.0[52]. Genomescope estimated the haploid genome size to be 1.04Gb using a diploid model (fig. S16), a better model fit (95%) than the tetraploid model (91%), which also vastly underestimated the haploid genome size (497 Mb). This finding was consistent with the smudgeplot produced by Genomescope, which also indicated diploidy (fig. S17). Genomescope also identified that the sample was highly

heterozygous (3.56%) which likely falsely-inflated the haploid genome assembly size through the inclusion of large heterozygous contigs (haplotigs) as distinct contigs. In order to remove one haplotig from each heterozygous pair, we used Purge_dups[28]. Purge_dups uses both read depth and sequence homology to identify and remove duplicated contigs or duplicated regions of a contig, and reduced our assembly size to 1.2Gbp (table S1). BUSCO version 5.1.3 (Benchmarking Universal Single-Copy Orthologs)[33] comparisons of original and reduced assemblies using the eukaryota odb10 dataset (table S1) demonstrated a two-fold reduction of duplicated BUSCO genes (from 233 to 115) with an increase in missing BUSCO genes of only zero to two.

The HiFi *de novo* assembly, purged of haplotigs, and Dovetail OmniC library reads were used as input data for HiRise, a software pipeline designed specifically for using proximity ligation data to scaffold genome assemblies[29]. Dovetail OmniC library sequences were aligned to the draft input assembly using bwa[53]. The separations of Dovetail OmniC read pairs mapped within draft scaffolds were analyzed by HiRise to produce a likelihood model for genomic distance between read pairs, and the model was used to identify and break putative misjoins, to score prospective joins, and make joins above a threshold (fig. S18). The NCBI[54] genome submission portal identified 16 contigs containing bacterial contamination (totalling 7.3 Mb) which were subsequently removed from the final assembly.

To assess the presence of remnant haplotigs and other assembly artifacts, we mapped Illumina reads used in the reference genome assembly to the haplotig-purged reference genome FASTA file using AdapterRemoval[55], BWA-MEM[53] and Picard MarkDuplicates (https://broadinstitute.github.io/picard/), and measured average sequencing depth and heterozygosity of the alignment in non-overlapping 1Mb windows across the genome. Window depth was never greater than two times higher or 0.5 times lower than the mean, and furthermore regions of both low depth and low heterozygosity were distributed throughout the genome. The fact that there were no large regions with both low read-depth and low heterozygosity points to the success of the haplotig removal (fig. S19). Minimap2 was used to align the genome against itself, after filtering for alignments less than 20kb and fewer than 1000 matches, to identify homologous blocks that may represent haplotigs. This analysis revealed no large syntenic blocks among scaffolds, further confirming the absence of recent allopolyploidy and the success of the haplotig removal (fig. S20).

519 **Whole-genome resequencing samples**

520 Whole-genome resequencing data used in this study have previously been described in Bieker
521 *et al.*[11]. Modern samples were field-collected between 2007 and 2019, and historic samples
522 were sequenced from herbarium specimens collected between 1830 and 1973. 121 modern
523 samples with corresponding phenotype data collected by van Boheemen, Atwater and
524 Hodgins[14] were used for genome-wide association studies. 284 modern samples (from
525 populations with a sample size >= 2) were used for environmental-allele associations. 97
526 historic and 100 modern samples divided into twelve populations were used for historic-modern
527 population comparisons (table S11). For ELF3 analysis, 26 samples from within 200km of Berlin
528 (15 historic and eleven modern) and 21 samples within 200km of Quebec City (ten historic and
529 eleven modern) were used. Genotyping and analysis of haploblocks was performed using 311
530 modern and 305 historic samples. For details of each sample see table S4.
531
532 **Sample alignment, variant calling and filtering**

533 FASTQ files from historic and modern *A. artemisiifolia* samples from North America and
534 Europe[11] were aligned to our new reference genome using the Paleomix pipeline[56], which
535 incorporates AdapterRemoval[55], BWA-MEM[53], Picard MarkDuplicates
536 (https://broadinstitute.github.io/picard/) and GATK IndelRealigner[57]. Mean depths of alignments
537 ranged from 0.33X to 18.03X with a mean of 3.67X for historic samples, and 1.60X to 39.80X
538 with a mean of 6.26X for modern samples (table S4). Variants were called in the higher-depth
539 modern samples using GATK UnifiedGenotyper[58]. GATK VariantFiltration[57] and VcfTools[59] were
540 used to filter variant calls. SNP and indel calls were separately filtered using GATK hard-filtering
541 recommendations (SNPs: QD < 2.0, FS > 60.0, SOR > 3.0, MQ < 40.0, ReadPosRankSum < -
542 8.0, MQRankSum < -12.5; indels: QD < 2.0, FS > 200.0, SOR > 10.0, ReadPosRankSum < -
543 20.0, InbreedingCoeff < -0.8). Additionally, SNPs and indels were separately filtered for sites
544 with depth (DP) less than one standard deviation below the mean, and greater than 1.5
545 standard deviations above the mean. Individual genotypes were set to missing if their depth was
546 less than three, then variants with greater than 20% missing across all samples were removed.
547 Samples with greater than 50% missing variants were removed. For the remaining 311 modern
548 samples, contigs with fewer than 100 variants were removed, and the remaining 30 contigs
549 were phased and imputed using Beagle 5.2[60].
550
551 **Genome annotation**

552 To obtain RNA transcript sequences for annotation of the genome, after 160 days of growth
553 additional samples of leaf, stem, flower, root, and branch were taken from individual “NSS02/B”

and flash-frozen in liquid nitrogen. From these we extracted RNA from seven tissues (young leaf, old leaf, stem, branch, and three stages of development of the floral head) using a Spectrum Plant Total RNA Kit (Sigma, USA) with on-column DNA digestion following the manufacturer's protocol. RNA extracts from all five tissues were pooled into a single sample. mRNA was enriched using oligo (dT) beads, and the first strand cDNA was synthesized using the Clontech SMARTer PCR cDNA Synthesis Kit, followed by first-strand synthesis with SMARTScribeTM Reverse Transcriptase. After cDNA amplification, a portion of the product was used directly as a non-size selected SMRTbell library. In parallel, the rest of amplification was first selected using either BluePippin or SageELF, and then used to construct a size-selected SMRTbell library after size fractionation. DNA damage and ends were then repaired, followed by hairpin adaptor ligation. Finally, sequencing primers and polymerase were annealed to SMRTbell templates, and IsoSeq isoform sequencing was performed by Novogene Europe (Cambridge, UK) using a PacBio Sequel II instrument, yielding 97,819,215 HiFi reads. To prepare the raw IsoSeq RNA data for downstream use in the annotation of the genome, we first identified the transcripts in the PacBio single-molecule sequencing data by following the IsoSeq v3 pipeline provided by PacificBiosciences (https://github.com/PacificBiosciences/IsoSeq). Briefly, the pipeline takes PacBio subread files as an input and undergoes steps of consensus generation, demultiplexing of primers, IsoSeq3 refinement, followed by a final clustering of the reads.

Prior to annotation of the genome, repetitive elements were identified using RepeatModeler2[61]. ProExcluder[62] was then run to remove any protein coding genes from the repeat library. RepeatMasker[63] was used to mask the genome using the finalized repeat library (table S2). A large fraction of the genome consisted of repetitive sequence (67%; fig. S1). Retroelements were the largest class (39.5%), with LTRs, particularly Gypsy (7.87 %) and Copia (18.98 %), the most prevalent retroelements.

Genome annotation was performed using the genome annotation pipeline MAKER2 version 2.31.9[36] with *ab initio* and homology-based gene predictions. 3,819 unique UniProtKB/Swiss-Prot protein sequences[64] from asterids (a monophyletic group of flowering plants), *Asteraceae* (sunflower family), and *Ambrosia* (ragweeds) were used for homology-based gene prediction. As no training gene models were available for *A. artemisiifolia*, we used CEGMA[65] to train the *ab initio* gene predictor SNAP[66]. MAKER2 was run with command-line arguments *model_org=simple*, *softmask=1*, *augustus_species=arabidopsis* and the *snaphmm* parameter

588 was set to the HMM generated in the manual training of SNAP. As expressed sequence tag
589 (EST) evidence, we used the IsoSeq clustered reads merged with a previously described
590 transcriptome[11].
591
592 A high confidence gene set of 29,849 gene models with strong protein or transcript support was
593 identified. These gene models had average coding lengths of 1.09 kb and 7.18 exons per gene
594 (table S3). Gene models were compared with *Arabidopsis thaliana* annotations (TAIR10
595 representative gene model proteins[67]) and the UniProtKB database using the *blastp* command
596 in BLAST+[68]. Using an E-value threshold of 1×10^{-6}, 26,688 (89.4%) genes matched TAIR10
597 annotations and 23,019 (78.1%) were matched UniProtKB (table S21). Gene ontology (GO)
598 enrichment was assessed using GO terms from *A. thaliana* TAIR 10[67] BLAST results. To
599 identify GO terms enriched among candidate lists, the R/topGO package[69] was used with
600 Fisher's exact test, the 'weight01' algorithm, and a p-value < 0.05 to assess significance.
601 Additionally, annotations were cross-referenced with 306 *A. thaliana* FLOR-ID flowering time
602 pathway genes[70]. 538 predicted *A. artemisiifolia* genes were matched to this dataset,
603 representing 212 unique FLOR-ID genes. Enrichment of flowering time genes was also
604 assessed in candidate gene lists using Fisher's exact test and a $p < 0.05$ threshold. The effects
605 of imputed variants on predicted genes were estimated using SnpEff[71].
606
607 **Allele frequency outliers and environmental allele associations**
608 Imputed genotype data from modern samples were divided for between-range and within-range
609 analyses in PLINK 1.9[72], and a minor allele frequency threshold of 0.05 was applied within data
610 subsets. For within-range analyses, sampling locations with fewer than two samples were
611 excluded and allele frequencies were calculated for each sampling location, resulting in 955,827
612 SNPs across 143 samples and 43 populations in North America and 941,649 SNPs across 141
613 samples and 31 populations for Europe. Allele frequency outliers were identified within each
614 range using the BayPass core model[39], with an Ω covariance matrix computed from 10,000
615 randomly-sampled SNPs that were located outside annotated genes and haploblocks, and
616 pruned for linkage disequilibrium using a window size of 50kb, a step size of 5bp and an r^2 of
617 0.5 in PLINK[72]. To identify allele frequency variation associated with environmental variables
618 within ranges, 19 bioclimatic variables were extracted for each sampling location from the
619 WorldClim database[40] using the R/raster package[73]. Associations with latitude and longitude of
620 sampling location, along with the 19 bioclimatic variables, were assessed for correlations with
621 population allele frequencies using Kendall's τ statistic in R[74]. Genome-wide XtX and τ results

were analyzed in non-overlapping 10kb windows using the weighted-Z analysis (WZA)[41], with the top 5% of windows designated outliers.

Genome-wide association studies

Imputed genotypes from modern samples were filtered in PLINK 1.9[72]. Non-SNP sites and sites with more than two alleles were removed. The 121 samples overlapping those phenotyped by van Boheemen, Atwater and Hodgins[14] were retained (table S4), and sites with a minor allele frequency below 0.05 were removed, resulting in 950,742 SNPs for analysis. Genome-wide association studies (GWAS) were performed across 121 individuals from both North American (n = 43) and European (n = 78) ranges using EMMAX[75], and incorporating an identity-by-state kinship matrix (generated in PLINK 1.9)[72] to account for genetic structure among samples. The kinship matrix was computed using 650,301 SNPs which remained after pruning for linkage disequilibrium using a window size of 50kb, a step size of 5bp and an r^2 of 0.5. Candidate SNPs were identified using a conservative threshold of Bonferroni-corrected p-values < 0.05.

Phenotypic analysis of herbarium specimens

We conducted a trait-based analysis of herbarium specimens found in the Global Biodiversity Information Facility database (gbif.org 2021). We compiled information from all *A. artemisiifolia* European herbarium specimens for which there was a digitized image of the individual in the database alongside corresponding metadata (location and collection date). The collection date spanned 1849 to 2020 (median 1975) and comprised 985 specimens. We determined the stage of flowering (no male inflorescence present, only immature male inflorescence present, mature male inflorescence present) for each image. The presence of fruit was also recorded. The male inflorescence was used as an indicator of flowering as these structures are more visually prominent than female flowers and the onset of male and female flowering is highly correlated[14]. Male florets consist of prominent spike-like racemes of male capitula, and are found at the terminus of the stem, whereas female florets are observed to be in inconspicuous cyme-like clusters and are arranged in groups at the axils of main and lateral stem leaves (fig. S4). The dates when the specimens were collected were converted to Julian day of the year. We conducted a generalized linear model with a binomial response and logit link (glm R). Both binary traits (presence of a mature male inflorescence; the presence of fruit) were included as response variables in two separate models. The significance of the effects were tested using the Anova function (Car package R)[76] using type 3 tests. For both models, the predictors of latitude, day of the year, and collection year as well as all interactions were included. Non-significant

656 interactions were removed in a stepwise fashion, starting with the highest order. Latitude of
657 origin strongly correlates with flowering time in common garden experiments[14] and we expected
658 northern populations to evolve early flowering relative to the start of the growing season to
659 match the shorter growing seasons in these areas. As a result, if local phenology has evolved to
660 better match the local growing season we predicted a collection year by latitude interaction, as
661 the relationship between latitude and the probability of flowering in wild collected accessions
662 should change over time when controlling for the day of collection.
663
664 **Historic-modern genomic comparisons**
665 To identify targets of recent selection, we compared historic and modern samples from twelve
666 locations (five locations from North America and seven from Europe; table S11). Historic
667 samples were grouped based on age of sample and proximity to a modern population. Analyses
668 were performed in ANGSD[77] using genotype likelihoods. For each population location we
669 calculated pairwise nucleotide diversity (θ_π) for historic and modern populations separately, and
670 F_{ST} between historic and modern populations at each location. Statistics were calculated in non-
671 overlapping 10kb windows, and windowed θ_π values were normalized by dividing by the number
672 of sites in each window. At each location, windows with θ_π more than two standard deviations
673 below the mean in both historic and modern populations were excluded from the analysis. We
674 identified putative selective sweeps in each population as windows with extreme shifts over time
675 in allele frequency as well as extreme reductions in diversity (i.e. windows in the top one percent
676 of both F_{ST} and $\theta_{\pi H}/\theta_{\pi M}$ distributions).
677
678 **Temporal allele frequency shifts in candidate loci**
679 In order to track allele frequency shifts over time, we estimated contemporary and historical
680 allele frequencies of the *ELF3* non-synonymous SNP and the haploblock HB448, which are two
681 candidate loci for recent selection in Europe. Both candidates showed evidence of local
682 selection using spatial analysis of modern populations, as well as sweep signals in temporal
683 comparisons of individual populations. These calculations were performed in geographic
684 regions where this recent selection is believed to have occurred at both historic and
685 contemporary timepoints. ANGSD (*-minMapQ 10 -minQ 5 -GL 2 -doMajorMinor 1 -doMaf 2 -*
686 *doIBS 1 -doCounts 1 -doGlf 2*) was used to calculate the allele frequency of the early flowering
687 *ELF3* allele (ScBFxKa_2:56025662) in 15 historic and eleven modern samples from within
688 200km of Berlin, whilst the frequency of HB448 in Europe was ascertained using haploblock
689 frequency estimates from across the European range (see below). To understand the

magnitude of these allele frequency shifts relative to putatively neutral alleles elsewhere in the genome, we calculated a standardized measure of frequency change, y_t, using estimates of historic, p_0, and contemporary, p_t, allele frequencies according to the equation:

$$y_t = \frac{p_t - p_0}{\sqrt{t p_0 (1 - p_0)}}$$

where *t* is the number of generations separating the frequency estimates (equivalent to the number of years due to ragweed's annual lifecycle). As we show in supplementary text S3, the distribution of y_t estimates under neutrality are predictable and roughly independent of the initial frequency of each neutral variant once the loci with low-frequency initial minor allele frequencies are filtered out. To further assess if selection was the likely cause of temporal changes of the *ELF3* and HB448 variants, we estimated the distribution of y_t estimates for computed from 10,000 randomly-sampled SNPs that were located outside annotated genes and haploblocks and pruned for linkage disequilibrium using a window size of 50kb, a step size of 5bp and an r^2 of 0.5 in PLINK 1.9[72]. Prior to calculation of y_t, sampled SNPs were then filtered for a minor allele frequency > 0.2 for HB448 comparisons and MAF > 0.05 for *ELF3* comparisons (due to the low historic frequency of *ELF3* in historic Berlin populations). We then compared the distributions to the y_t values of candidate adaptation loci to test whether candidate regions were more divergent than the putatively neutral distribution. As a point of comparison we repeated this analysis for the *ELF3* allele in Quebec. As in Berlin, this allele is at high frequencies, but substantial temporal change was not expected as the populations were predicted to be closer to the equilibrium over the temporal sampling period in the native range. Samples within 200km of Quebec City (ten historic and eleven modern) were pooled at both timepoints. Allele frequency changes of the 10,000 randomly-sampled SNPs and the non-synonymous *ELF3* allele were assessed as above.

Haploblock identification

To identify signatures of large, segregating haploblocks across the genome, we performed local windowed principal component analysis with Lostruct[45]. Using SNP data from 311 modern samples, we extracted the first ten multidimensional scaling (MDS) coordinates across each of the 30 imputed scaffolds (scaffolds with > 100 SNPs remaining after filtering) in windows of 100 SNPs. These MDS coordinates were then plotted along each scaffold to observe regions of local structure, indicative of segregating haploblocks. We focused on outlier MDS signals that

overlapped parallel outlier windows for both XtX and at least one environmental variable, and also showed well-defined boundaries indicative of chromosomal inversions. We tested for additional evidence of inversions using PCA of MDS outlier regions and kmeans clustering in R[74] to identify regions containing three distinct clusters representing heterozygotes and two homozygotes. Additionally, we assessed heterozygosity from genotype data in each haploblock region and in each modern sample, and measured linkage disequilibrium (the second highest r^2 value in 0.5Mb windows) across each scaffold bearing a haploblock for all modern samples and for modern samples homozygous for the more common haploblock genotype using scripts from Todesco *et al.*[26].

Haploblock frequency changes over time and space

For seven candidate inversions, a local PCA of each region and kmeans clustering was then repeated in PCAngsd[78], so as to allow genotype estimation of these haploblocks in 305 historic samples alongside the 311 modern samples. For this local PCA we used sites diagnostic of the haplotypes (with F_{ST} values > 0.1 between the identified homozygote clusters in modern samples, using vcftools v0.1.15 –weir-fst-pop (Auton and Marcketta, 2009) confined to the haploblock coordinates) to reduce clustering ambiguity which was heightened by the low coverage historic samples. We also conducted a PCA on 10,000 SNPs randomly-sampled from the 311 modern genomes that were located outside annotated genes and haploblocks, and pruned for linkage disequilibrium using a window size of 50 kb, a step size of 5 bp and an r^2 of 0.5 in PLINK[72]. Following this, we used generalized linear models (glm R) to assess how haplotype frequency (binomial response) changed over time and space. A count of each haplotype at a geographic location and year was the binomial response variable and time period (historic or modern), range (North America or Europe), latitude, and all interactions between these three main effects were used as predictors. Non-significant interactions were removed in a stepwise fashion, starting with the highest order. PC1 from the PCA of 10,000 randomly-sampled SNPs was included as a covariate to control for the effects of population structure on haplotype frequency. We tested the significance of the effects in our model using the Anova function (Car package R)[76] with type 3 tests. Significant differences among groups for means or slopes were tested with the emmeans package using an FDR correction[79]. To determine if the classification of samples into modern or historic timepoints influenced our results we ran a second set of generalized linear models examining haplotype frequency as a function of collection year, range (North America or Europe), latitude, and all interactions between these three main effects as well as PC1, using the same approach as above. For interactions

757 involving two continuous variables (i.e., latitude and year) we tested if the slope estimates of
758 one variable were significant at specific values of the other using the package emmeans. This
759 allowed us to estimate when and where the haplotype frequencies were changing. The results
760 from both approaches (time as two categories or time as continuous) provided qualitatively
761 similar patterns.
762
763 We estimated the relative strength of selection on haploblocks along the latitudinal clines in
764 modern North American and European populations using slopes from logistic regressions (see
765 supplementary text S2). Specifically, we used generalized linear models to estimate the slopes
766 of the regression for each range and time point (modern or historic) combination (group). A
767 count of each haplotype at a geographic location was the binomial response variable and time
768 period (historic or modern), range (North America or Europe), latitude, and all interactions
769 between these three main effects were used as predictors. All interactions were retained in the
770 model and slopes and their confidence intervals estimated for each group using the function
771 emtrends (emmeans package R[79]; table S13). PC1 was included as a covariate to control for
772 the effects of population structure on haplotype frequency. We expected the slopes to be
773 shallower in the historic versus the modern European group, but similar across timepoints in
774 North America. To test this, we used a t-test and compared slopes for modern and historic
775 timepoints in each range. We also expected that the magnitude of change in the slope over time
776 would be the greatest in haploblocks showing the largest estimates of selection in Europe (table
777 S15). We estimated the relative strength of selection for the modern European range for each
778 haploblock and tested if the change in slope for each haploblock was correlated with this
779 estimate. We also examined if there was a correlation in the relative strength of selection for
780 modern North American and European haploblocks, which would indicate parallel selection
781 along the cline in each range.
782
783 We compared our slope estimates of the haploblocks to the genome wide distribution in each
784 range using 10,000 randomly selected SNPs outside of genes and haploblocks. We did this to
785 determine if our haploblocks showed stronger latitudinal patterns than the majority of SNPs, in
786 one or both ranges, which may be indicative of spatially varying selection. For the modern
787 samples in each range (North America or Europe), we fit a generalized linear model with latitude
788 as the only predictor. We did this for each null SNP and each haploblock that was statistically
789 associated with latitude.
790

Recombination rates in haploblocks

The haploblocks show multiple genomic signatures of reduced recombination. To confirm this we analyzed recombination rates in genetic maps. Further if the haploblocks were caused by global reductions in recombination rate (e.g., the region was found in an area with generally low recombination such as a centromere), all maps should show reduced recombination rates. However, if inversions were the cause, recombination would only be suppressed in genotypes heterozygous for the inversion, while homozygous individuals would not show suppressed recombination. To determine if there were genotype-specific reductions in recombination rate in the seven candidate haploblocks, which would be consistent with inversions, we made use of three previously generated genetic maps[42]. Markers were generated using genotype by sequencing and alignments to the new reference. Details of the sequencing, alignments and variant calling can be found in Prapas *et al.*[42]. We developed sex-specific genetic maps (i.e., maps for the maternal and paternal parent) using Lep-MAP3[80] for each scaffold of interest and in each mapping population (an F1 mapping population and two F2 mapping populations). Multiple maps were constructed since the haploblocks may have been segregating in different frequencies in the parents of the mapping populations derived from outcrossing. Linkage map construction was constrained by the physical order of the markers along each scaffold of interest. Genetic distance (cM) was plotted against physical position along the chromosome for each map and the intervals of the QTL and the boundaries of the haploblocks were visualized and inspected for reduced recombination compared to the rest of the scaffold.

ACKNOWLEDGEMENTS

We thank Greg Owens & Michael Whitlock for discussions, and Samuel Yeaman and Sarah Otto for feedback on the manuscript. We are grateful to François Bretagnolle, Myriam Gaudeul, Heinz Mueller-Schaerer, Gerhard Karrer, and Bruno Chauvel for their assistance in obtaining many of the samples upon which this study is based, and Marie Brunier, Fátima Sánchez Barreiro, Yohann Roy, Luna Forcioli, Jacqueline Y. Lee for assistance during lab work. Some sequencing services were provided by the Norwegian Sequencing Centre, a national technology platform hosted by the University of Oslo. Some sequencing was performed by the NTNU Genomics Core Facility. Genome scaffolding was performed by Dovetail Genomics. Some analyses were performed on resources provided by Sigma2, MASSIVE M3 and ComputeCanada high performance computing platforms. We kindly thank the curators from the following herbaria for allowing us to destructively sample their precious collections: B, BR, BRNU, C, FI, G, GH, GOET, GZU, HBG, I, IASI, JE, L, LD, LY, MARS, MASS, MO, MPU, NEBC, NEU, NY, P, PH, PR, PRA, PRC, QFA, S, STU, TRH, UPS, US, W, WU.

FUNDING

This research received support from an NTNU Onsager Fellowship award, Norwegian Research Council Young Research Talents award 287327, and a SYNTHESYS Project award (www.synthesys.info, financed by European Community Research Infrastructure Action under the FP7 "Capacities" Program) to M. D. M., a FORMAS (2016-00453) & Carl Trygger Foundation for Scientific Research (grant CTS 14.425) to R. S., and an ARC DP220102362 and DP180102531 and HFSP RGP0001/2019 to K. A. H .

AUTHOR CONTRIBUTIONS

Paul Battlay: Software, Formal analysis, Investigation, Data curation, Writing - Original draft, Writing - Review and editing, Visualization **Jonathan Wilson:** Software, Formal analysis, Investigation, Visualization **Vanessa C. Bieker:** Software, Investigation, Data curation **Chris Lee:** Investigation, Resources **Diana Prapas:** Software, Formal analysis **Bent Petersen:** Software **Sam Craig:** Investigation **Lotte van Boheemen:** Investigation, Resources **Romain Scalone:** Resources **Nissanka P. de Silva:** Software, Visualization **Amit Sharma:** Investigation, Resources **Bojan Konstantinović:** Investigation, Resources **Kristin A. Nurkowski:** Investigation, Resources **Loren Rieseberg:** Writing - Review and editing **Tim Connallon:** Methodology, Formal analysis, Investigation, Writing - Original draft, Writing -

Review and editing **Michael D. Martin:** Conceptualization, Methodology, Resources, Writing - Review and editing, Supervision, Project administration, Funding acquisition **Kathryn A. Hodgins:** Conceptualization, Methodology, Software, Formal analysis, Investigation, Resources, Writing - Original draft, Writing - Review and editing, Supervision, Project administration, Funding acquisition, Visualization

COMPETING INTERESTS

The authors declare no competing interests

DATA AND CODE AVAILABILITY

Sequences used in reference genome assembly and annotation are available from NCBI under BioProject ID PRJNA819156 (to be released upon publication; reviewer link: https://dataview.ncbi.nlm.nih.gov/object/PRJNA819156?reviewer=ppu225pmsn5tbfvf04s3tadkfj) . Reference genome FASTA and annotation GFF files are available from FigShare (to be released upon publication). Individual sample resequencing data are available from ENA under BioProject IDs PRJEB48563, PRJNA339123 and PRJEB34825.

SUPPLEMENTARY FIGURES

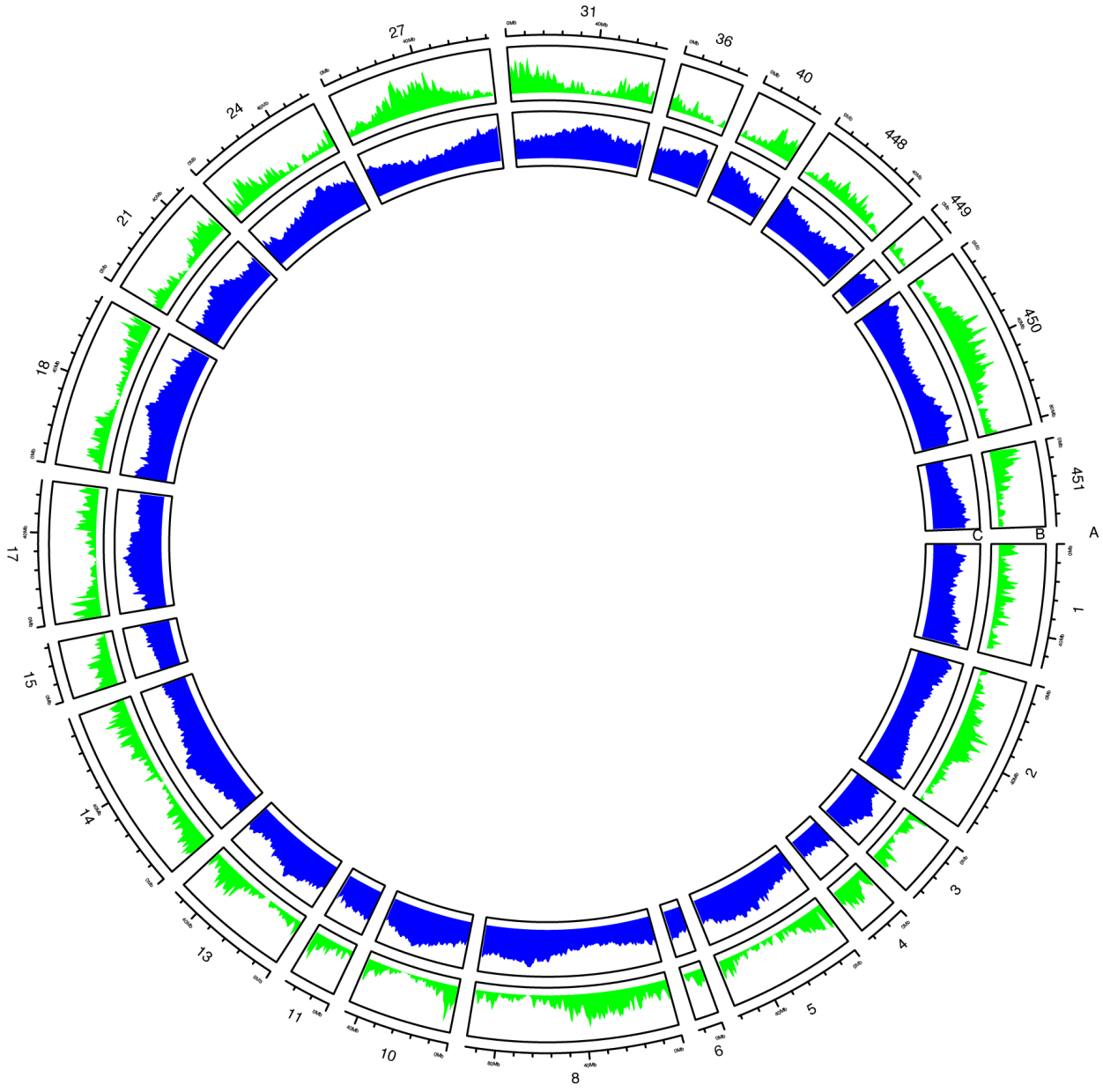

Figure S1. The *Ambrosia artemisiifolia* genomic landscape location across the 24 scaffolds greater than 10Mb in length (track **A**), and the distribution, in 1Mb windows of gene density (track **B**) and repeat density (track **C**).

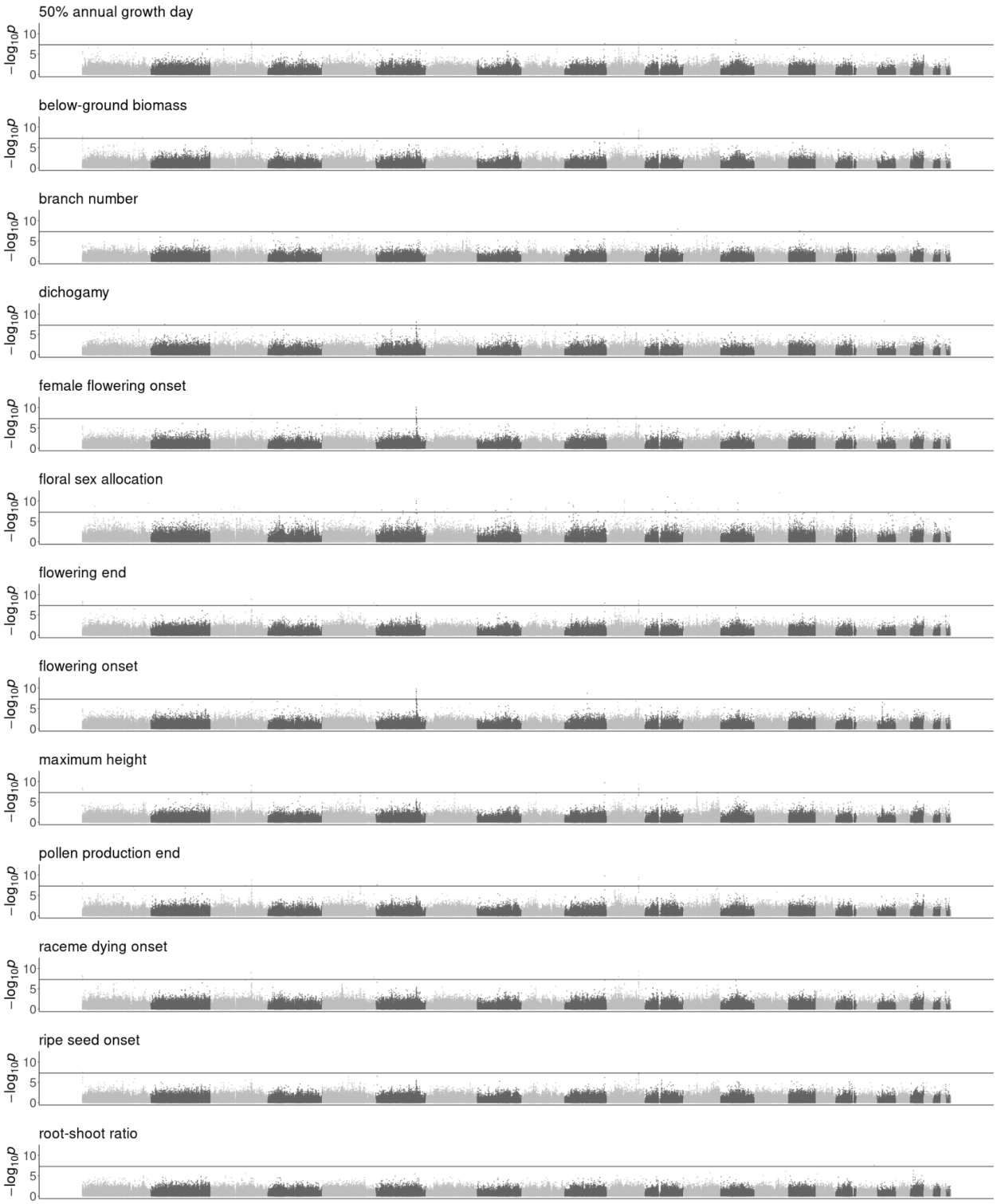

Figure S2. Genome-wide association study results for phenotypes with significant SNPs. Solid lines indicate a Bonferroni-corrected significance threshold of 0.05.

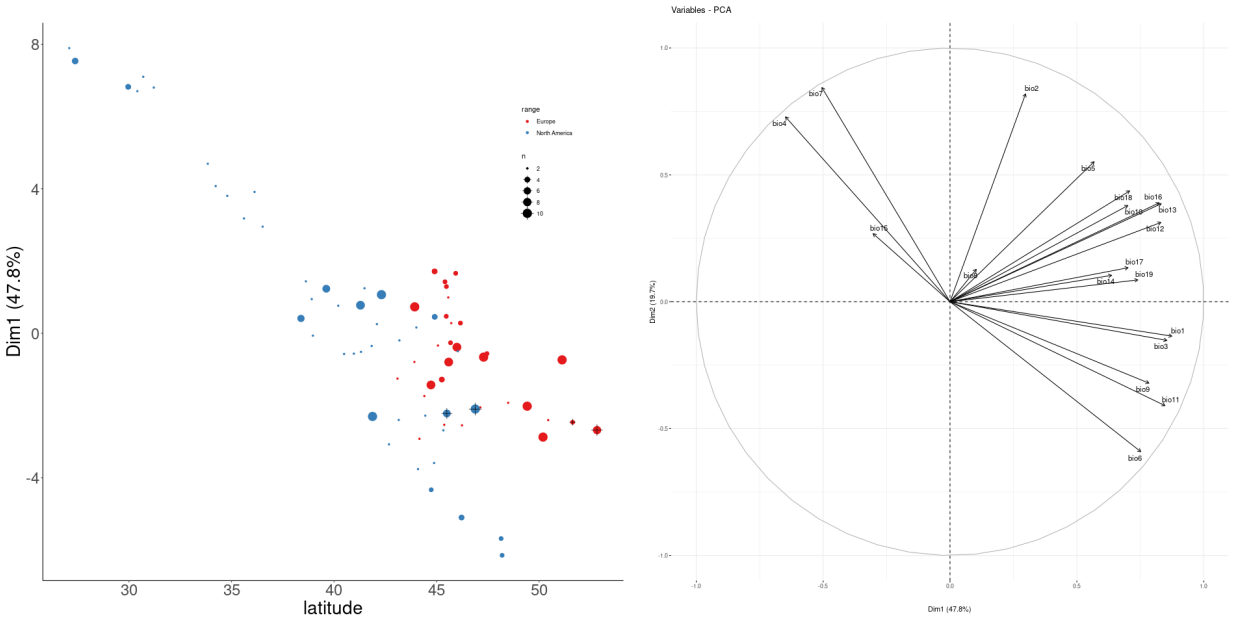

Figure S3. Environmental comparison of North American and European *A. artemisiifolia* ranges. The left pane shows the first principle component of 19 bioclimatic variables against latitude for modern ragweed populations in North America (red) and Europe (blue). Crosses identify the populations with high *ELF3* allele frequencies. The right pane shows a variable correlation plot for 19 bioclimatic variables.

873

874 **Figure S4.** An example herbarium specimen of *Ambrosia artemisiifolia* (left) and a detail (right)

875 showing the mature male inflorescence (solid line) and seeds (dashed lines).

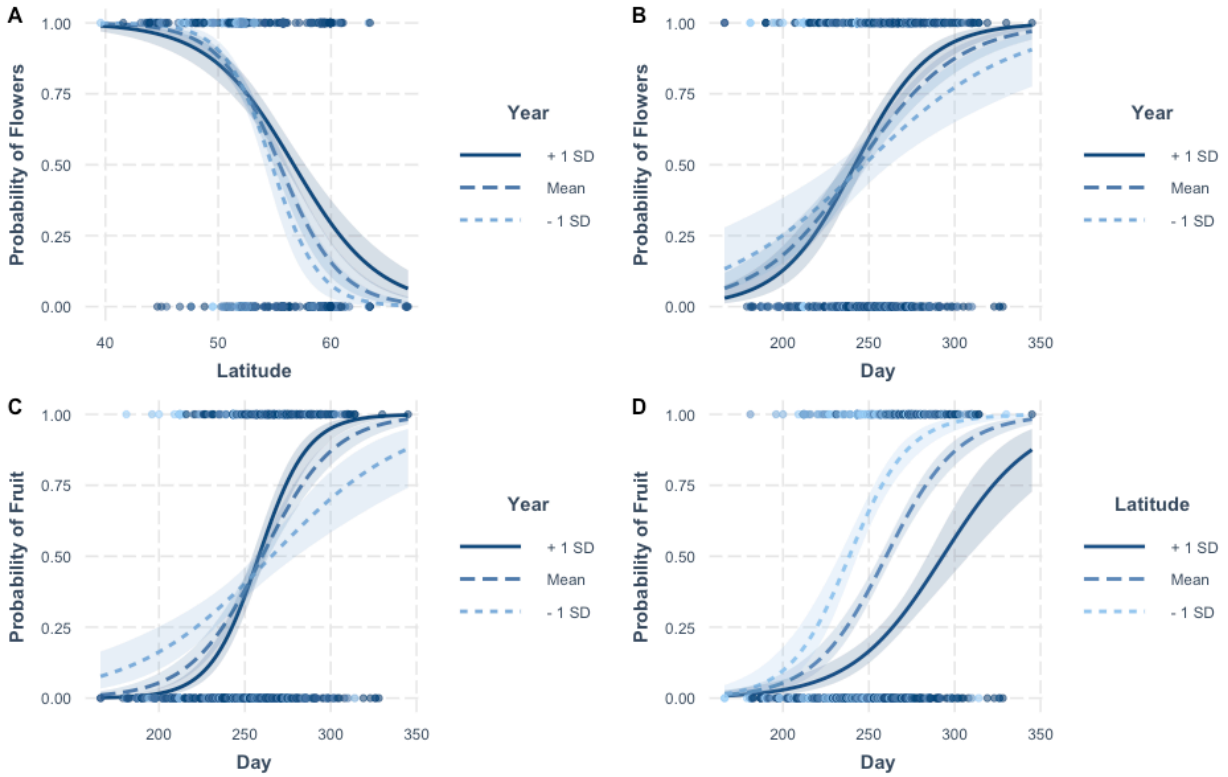

Figure S5. Interaction plots illustrating the results of generalized linear models examining the presence of mature male inflorescences (probability of flowers) or mature fruit (probability of fruit) in herbarium specimens of *A. artemisiifolia* in Europe as a function of collection day (Day), latitude of origin (Latitude) and collection year (Year). The predicted probability of observing flowers is plotted as a function of latitude (**A**), or collection day (**B**) for different collection years (mean collection year +/- 1 SD). The predicted probability of observing fruit is plotted against collection day for different collection years (mean collection year +/- 1 SD; **C**) or latitudes (mean collection latitude +/- 1 SD; **D**). Confidence intervals for the predictions are shown as are the raw data.

Figure S6. Distributions of F_{ST} and $\theta_{\pi H}/\theta_{\pi M}$ between historic and modern samples from North American populations, and F_{ST} against genomic location. Red points indicate putative selective sweep windows, which are in top one percent of per-window F_{ST} and $\theta_{\pi H}/\theta_{\pi M}$ (dashed lines).

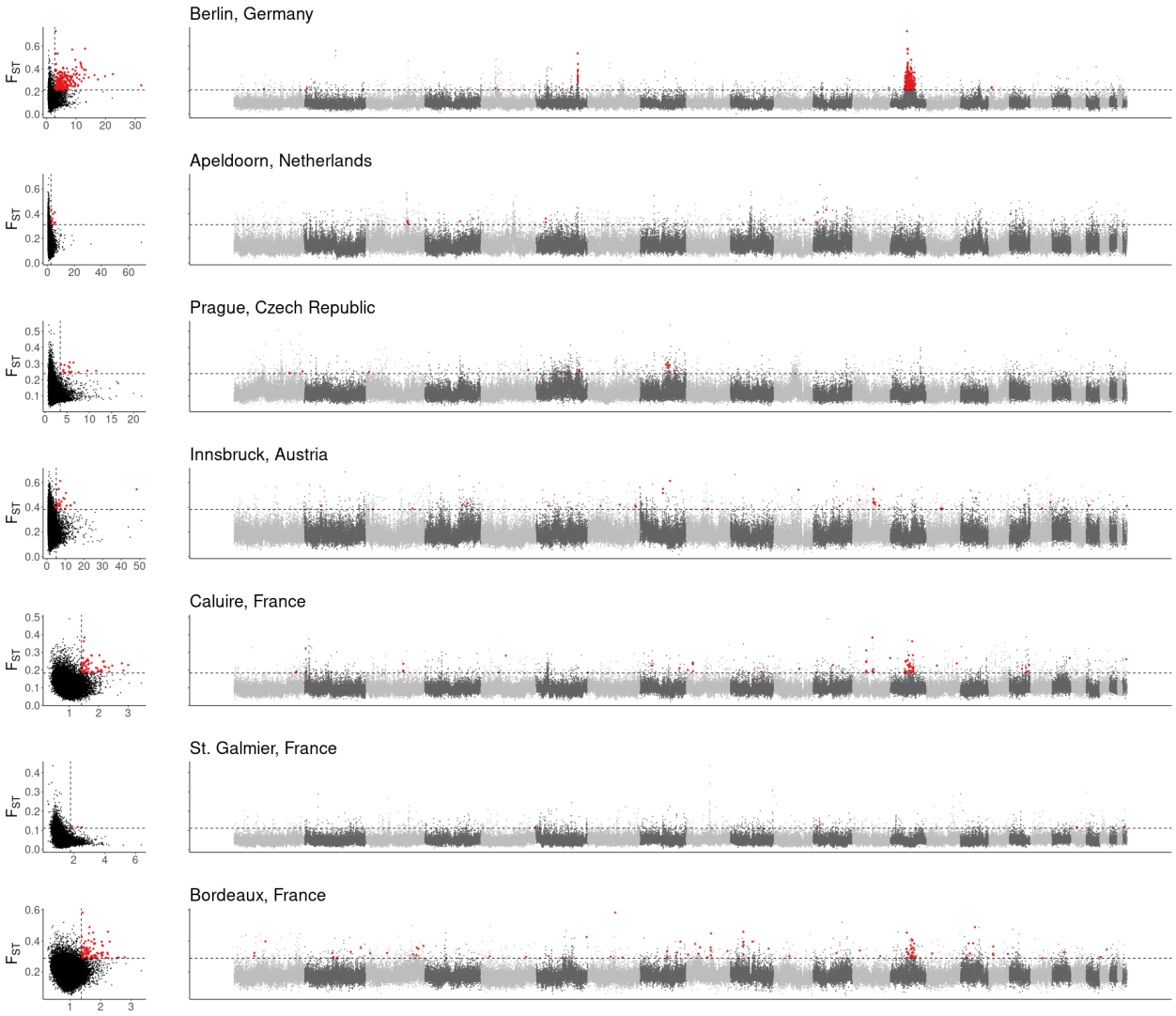

Figure S7. Distributions of F_{ST} and $\theta_{\pi H}/\theta_{\pi M}$ between historic and modern samples from European populations, and F_{ST} against genomic location. Red points indicate putative selective sweep windows, which are in top one percent of per-window F_{ST} and $\theta_{\pi H}/\theta_{\pi M}$ (dashed lines).

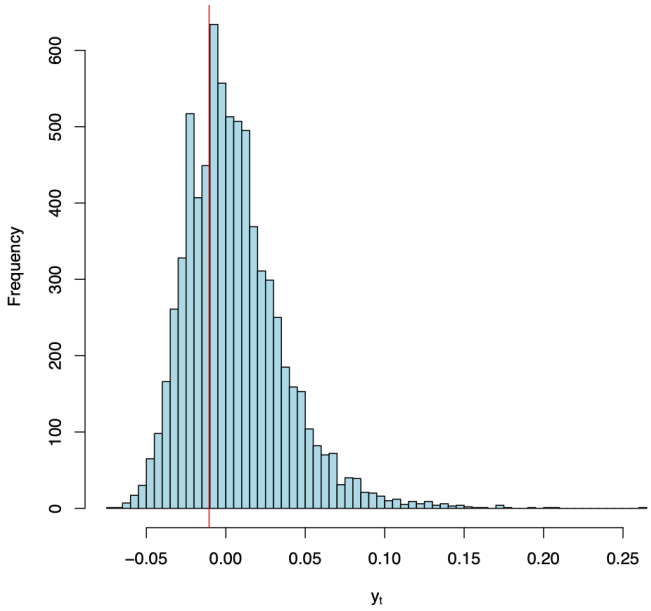

Figure S8. Distributions of y_t values (calculated according to equation 1) for allele frequency shifts in 10,000 putatively neutral SNPs (histogram) between historic and modern samples from within 200km of Quebec City. Red line indicates the y_t value for scaffold 2 position 56,025,662, a nonsynonymous SNP in *ELF3*.

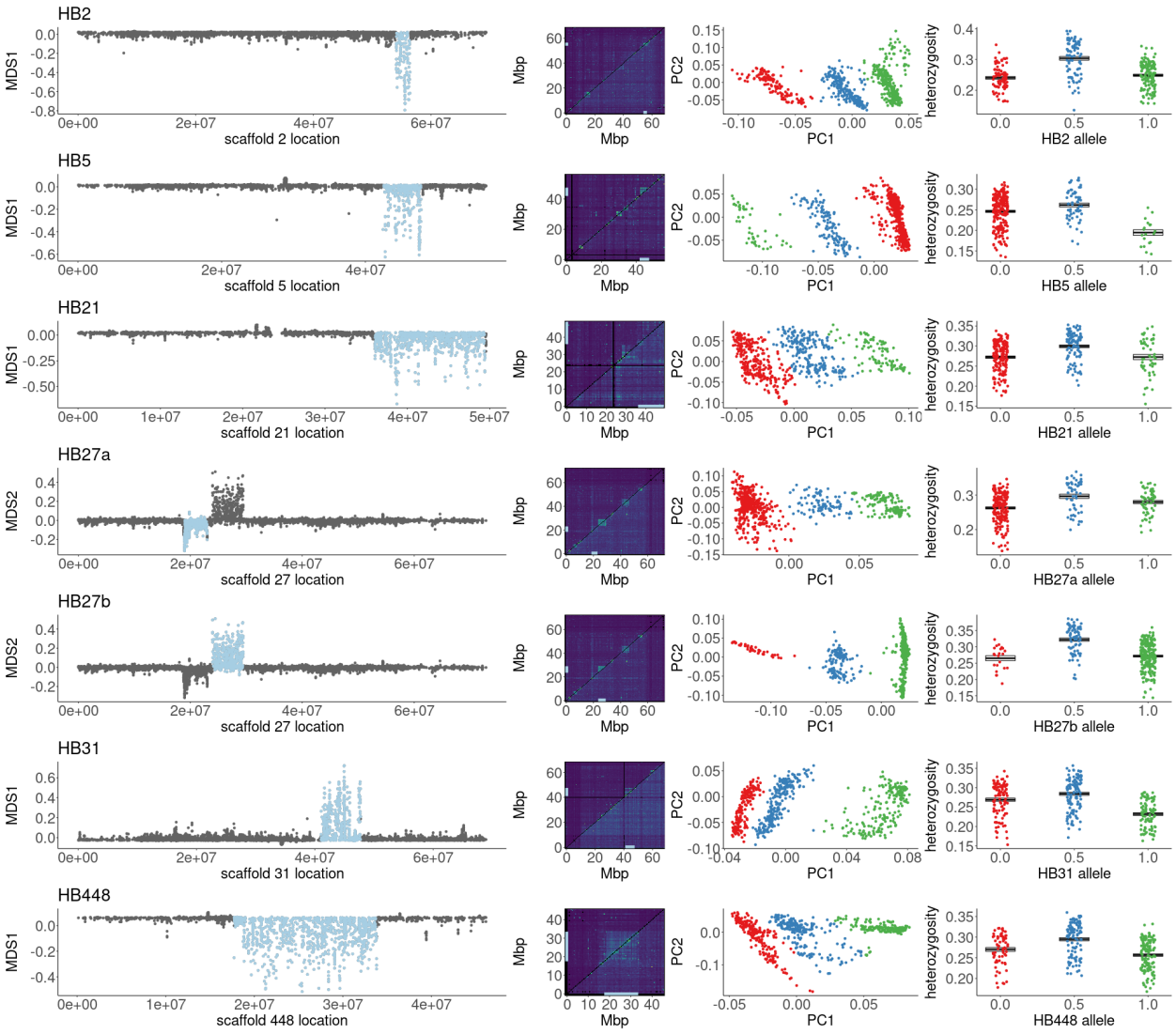

Figure S9. Haploblocks display extreme, divergent, local population structure (pale blue regions; first column). Haploblock regions (indicated by pale blue lines; second column) correspond to blocks of linkage disequilibrium (second highest r^2 in 0.5Mb windows) apparent using all modern samples (top triangle) but often reduced or absent using only samples homozygous for the more common haploblock genotype (bottom triangle). Haploblock genotypes were assigned by kmeans clustering (colours; third column) using the first two principal components of genetic variation across haploblock regions. Heterozygous haploblock genotypes show elevated mean per-site heterozygosity (fourth column; boxes denote mean and SEM).

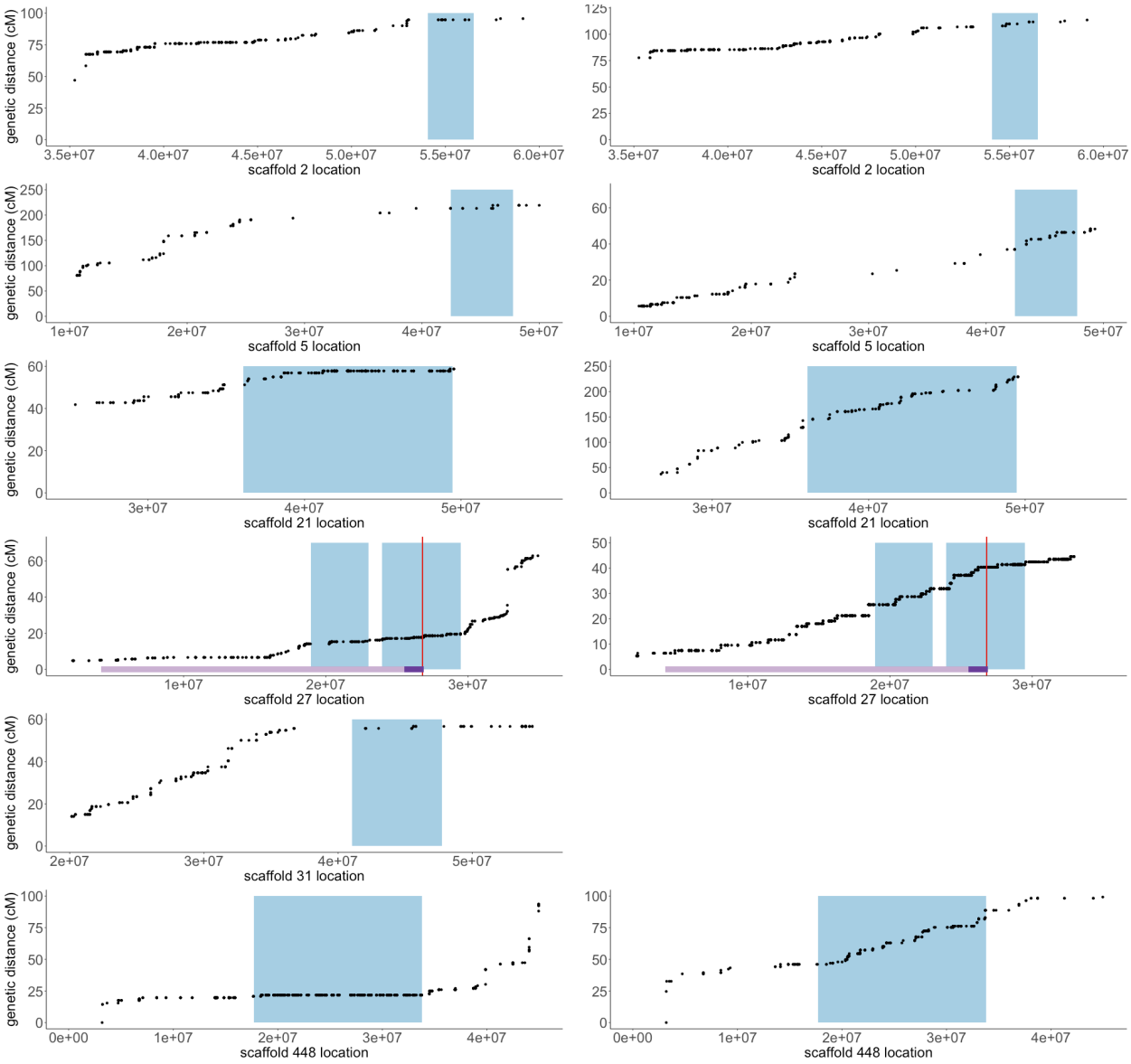

Figure S10. Evidence of genotype-specific reductions in recombination in haploblock regions. Genetic distance (cM) against physical distance (bp) along a portion of each scaffold is shown. Haploblock regions are shown in pale blue. Example maps are displayed showing both low recombination rates (left) and high recombination rates (right) for each haploblock (scaffold 31 had few markers within the haploblock for most maps, and there was no clear evidence of substantial recombination within the haploblock for any of the maps). For scaffold 27, QTL-mapping data from Prapas *et al.*[42] is shown: The marker closest to the large-effect flowering time QTL is represented by the red line. The 95% confidence intervals for male flowering time (dark purple), and height (light and dark purple) are indicated below the plots.

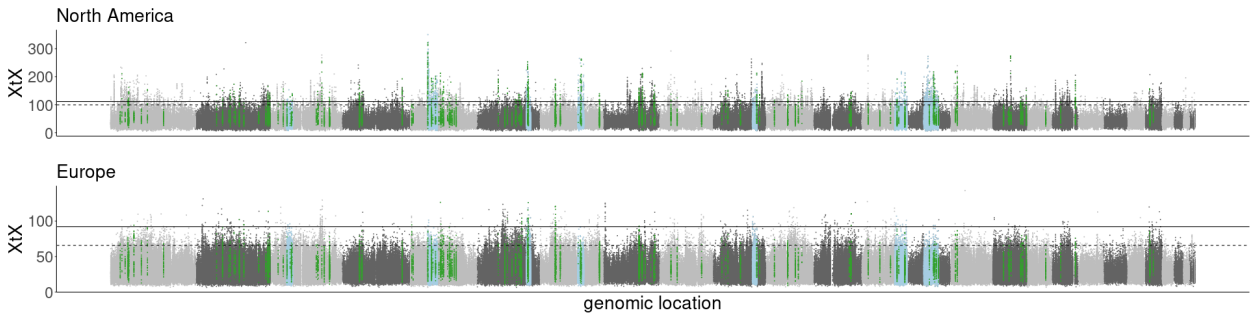

Figure S11. Genome-wide XtX scans between sampling locations within each range separately. Solid lines indicate Bonferroni-corrected significance derived from XtX *p*-values; dashed lines indicate the top 1% of genome-wide XtX values. Dark green highlights represent 10kb WZA windows with a top 5% WZA score in both ranges for XtX and at least one environmental variable. Pale blue highlights indicate haploblocks that overlap parallel WZA windows.

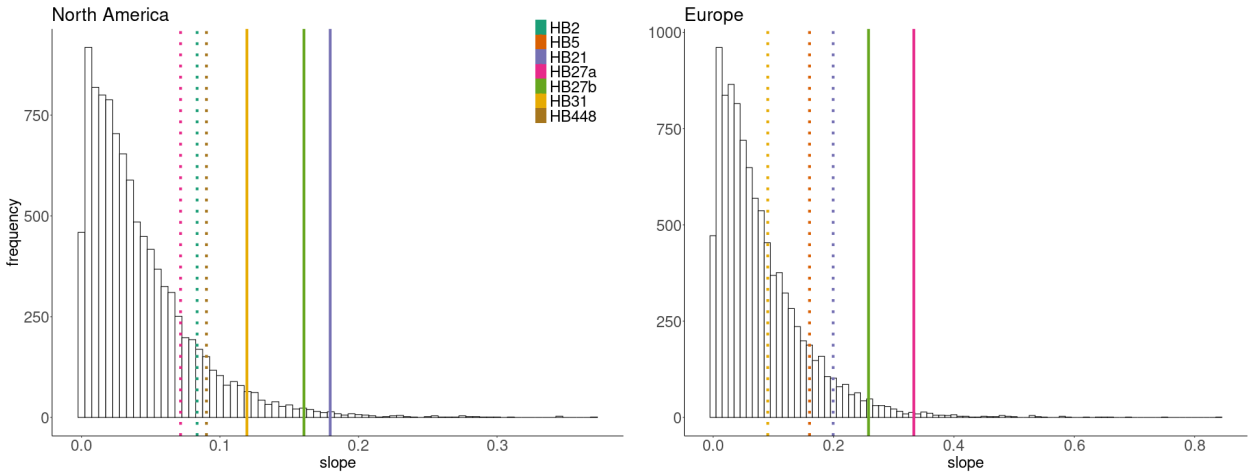

Figure S12. The distribution of slope estimates from generalized linear models of population allele counts against latitude for 10,000 randomly selected SNPs in each range. The vertical lines show the slope estimates for haploblocks with statistical associations with latitude in one range (table S12). Solid lines represent estimates in the 5% tail of each distribution while dotted lines fall below that cut-off.

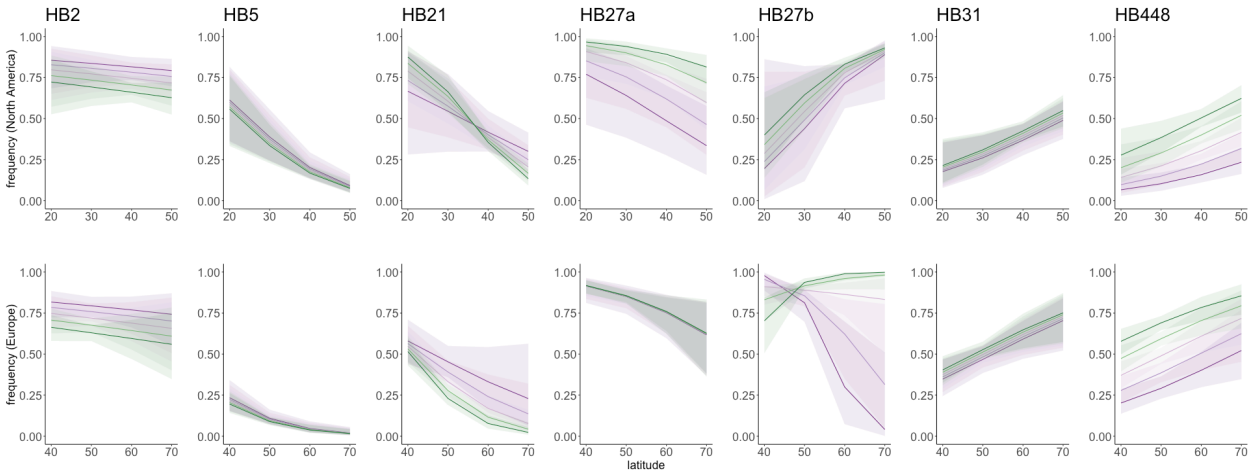

Figure S13. Logistic regression models with 95% CI ribbons (see table S12-S17 for model details) of haploblock frequency (allele 1) against latitude for each haploblock across five time bins ranging from most historic (purple) to most modern (green).

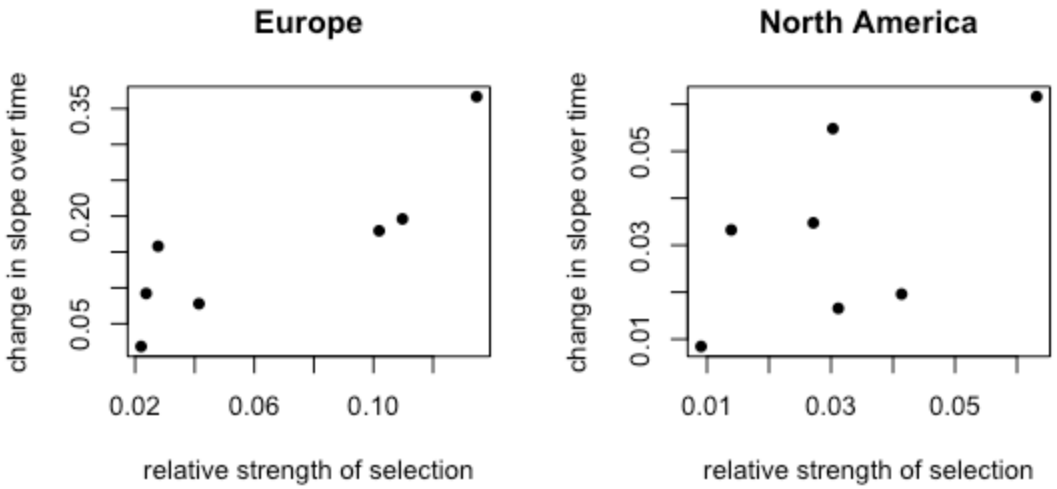

Figure S14. The change in the slope of the relationship between latitude and haplotype frequency (see table S15) between historic and modern samples compared to the estimate of selection along the latitudinal cline for the seven haploblocks (estimated from modern data in each range). A strong relationship was detected in the invasive European, but not the native North American range.

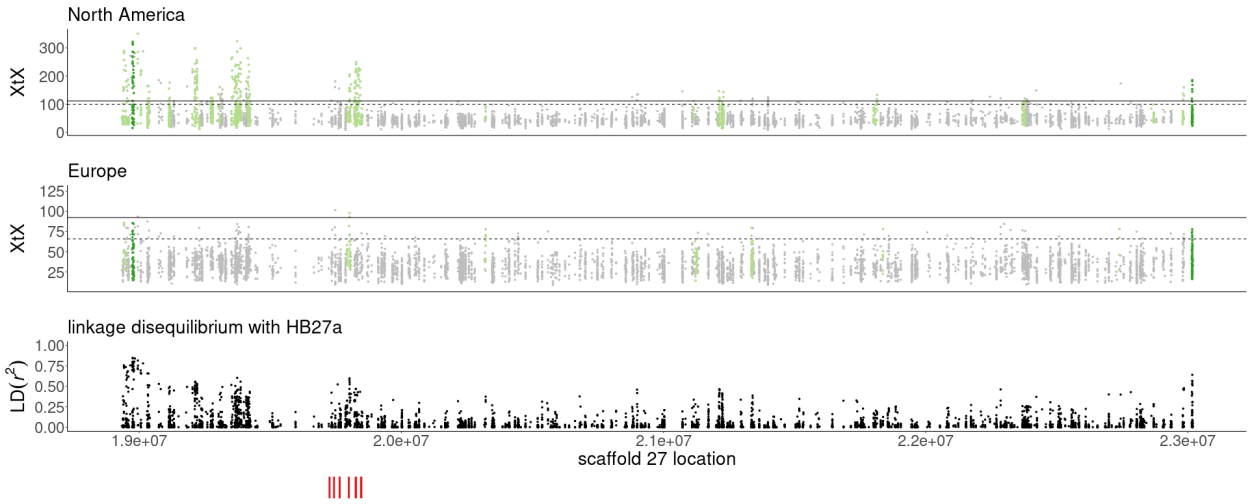

Figure S15. HB27a region (ScBFxKa_27:18930440-23019032). XtX and XtX-EAA outlier windows zoomed from fig. 1C, and linkage disequilibrium (r^2) between SNPs in the region and HB27a haploblock genotype. A cluster of pectate lyase genes, consisting of the top BLAST hit for *Amba1* and closely-related paralogues, are indicated in red below.

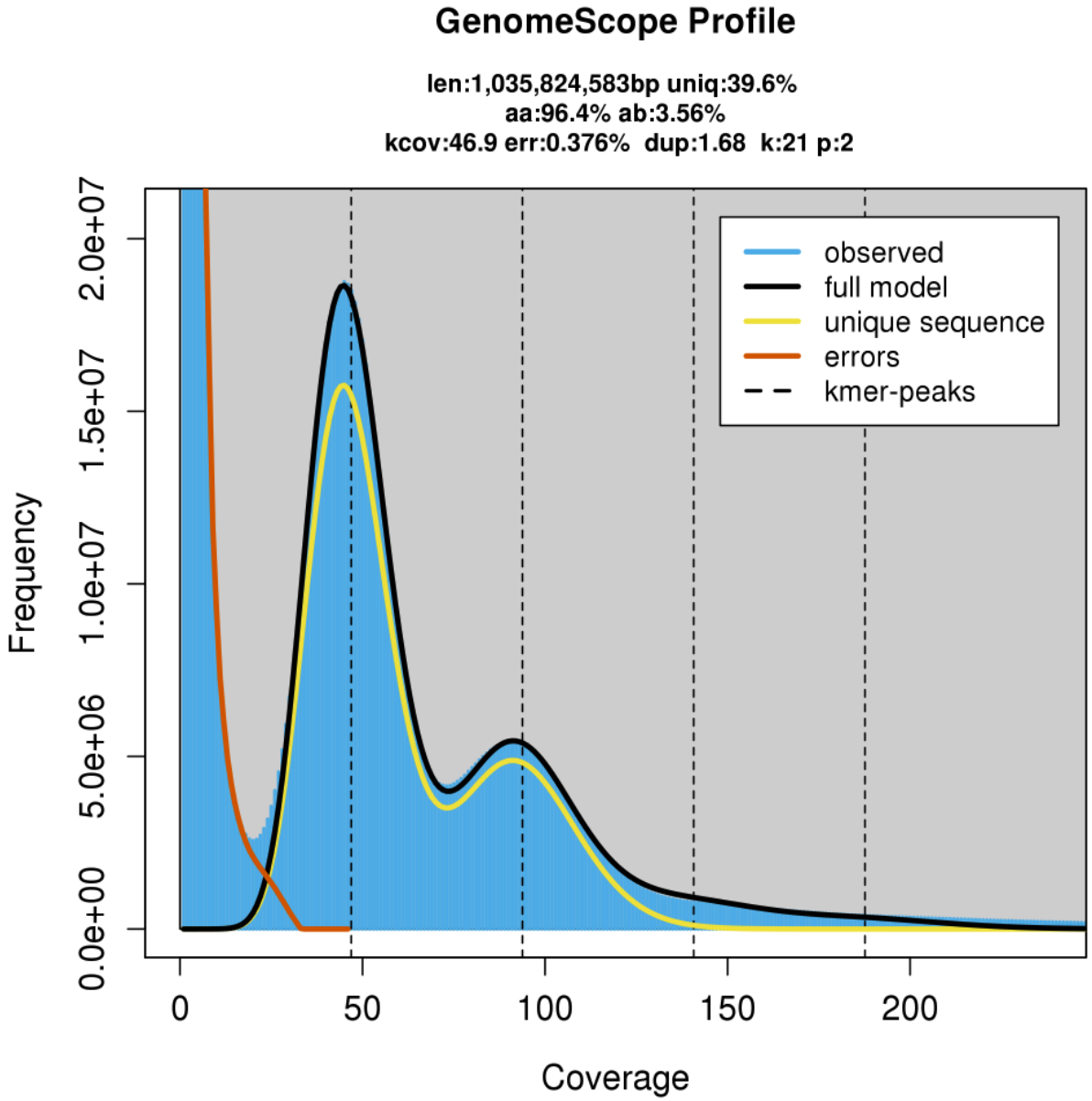

942

943 **Figure S16.** The kmer coverage and model fit from GenomeScope 2.0 for 21mers from the PacBio HiFi

944 and OmniC Illumina reads for *Ambrosia artemisiifolia.*

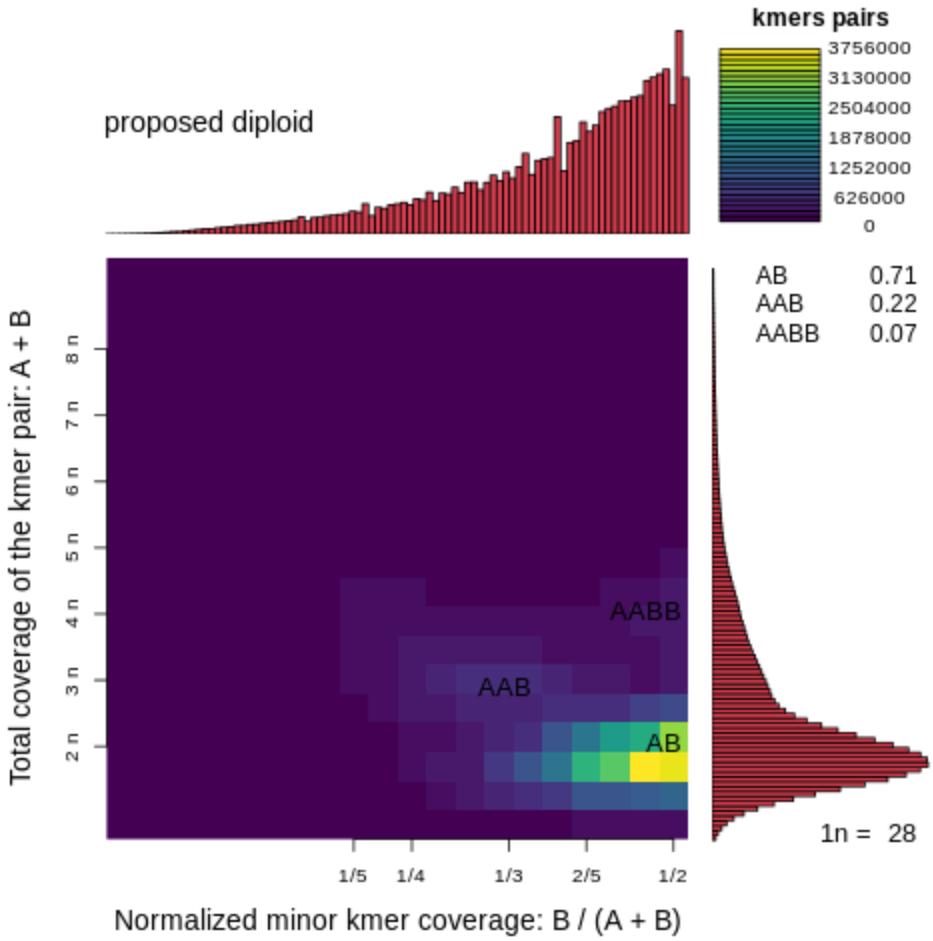

945

946 **Figure S17.** A smudgeplot for *Ambrosia artemisiifolia* used to estimate ploidy from heterzygous kmer

947 pairs using 21mers from the HiFi reads.

948

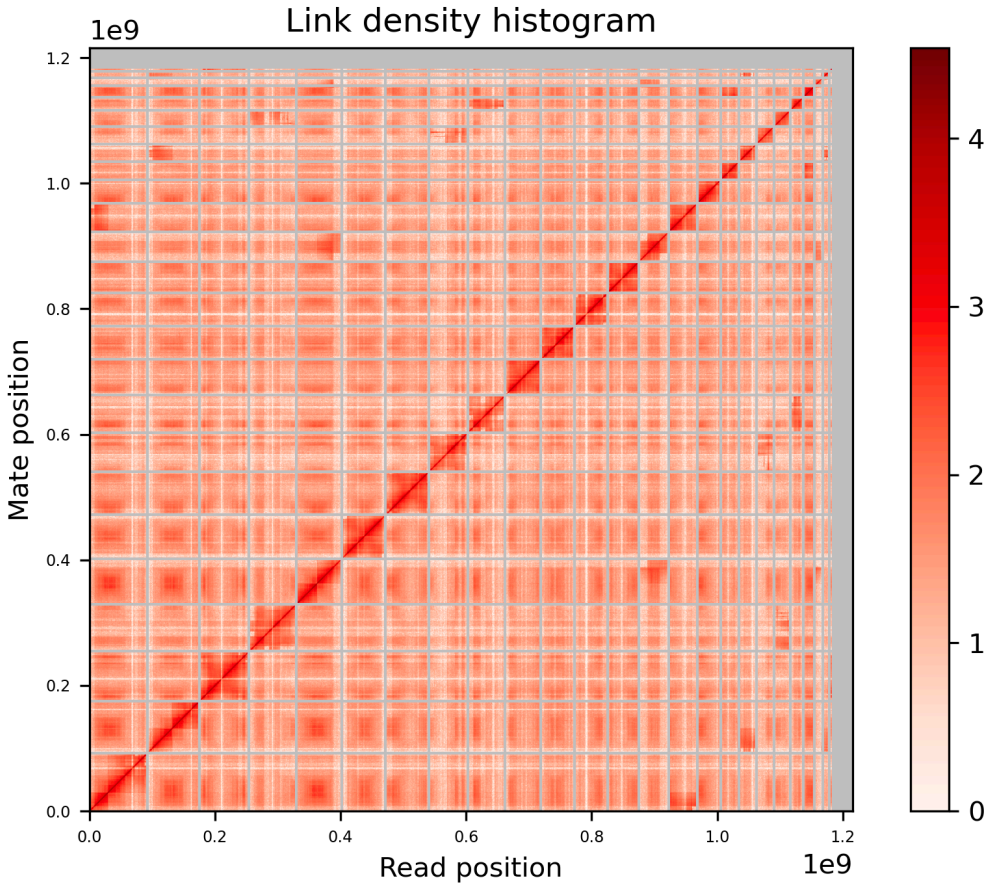

Figure S18. A link density histogram, identified by proximity ligation sequencing. The *x* and *y* axes show mapping positions of the first and second read in read pairs.

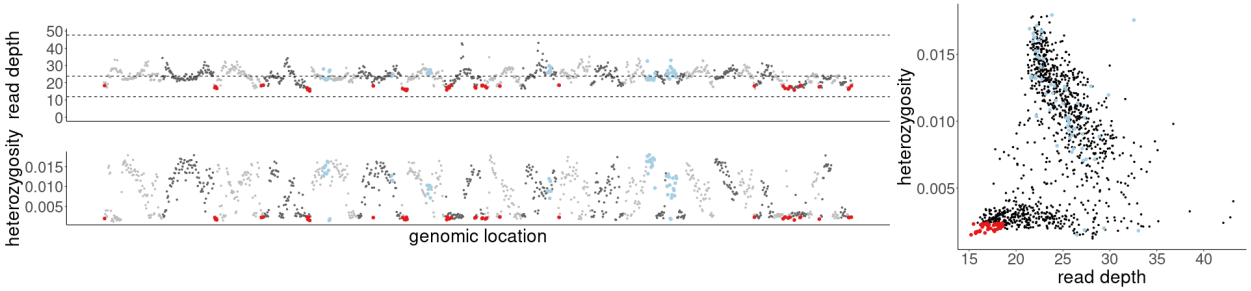

Figure S19. Read depth and heterozygosity in 1Mb windows for Illumina reads used in the reference genome assembly mapped to the final version of the reference genome. Windows in the bottom 10% of read depth and heterozygosity values are indicated in red; windows overlapping haploblocks are indicated in pale blue.

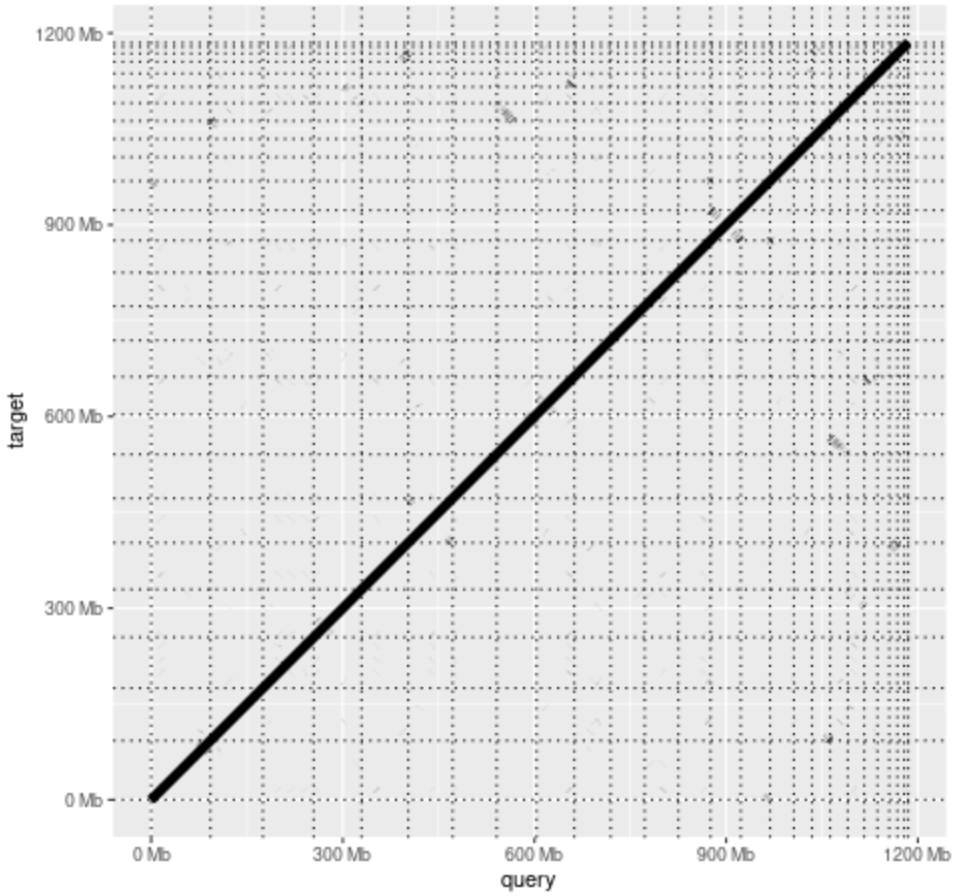

957

958 **Figure S20.** A dot plot of an alignment of the reference *Ambrosia artemisiifolia* genome against itself.

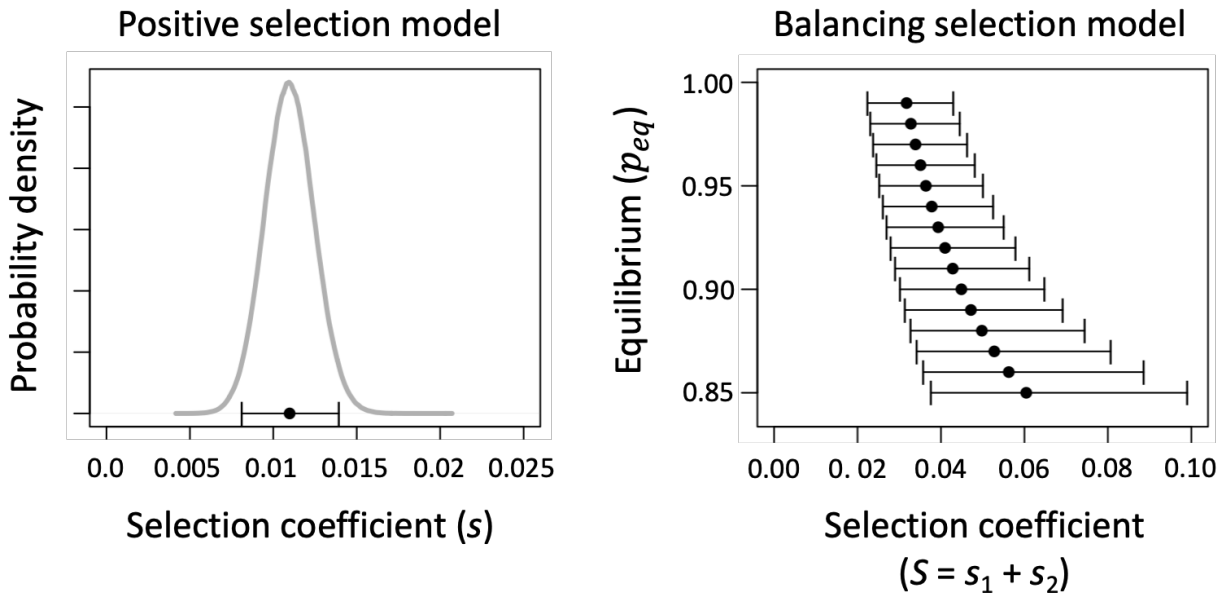

Figure S21. Selection coefficients consistent with observed frequency changes of the HB448 haplotype, under models of positive selection (left) and balancing selection (right). The left-hand panel shows the distribution of *s* values (gray) and the 95% CI for *s* (in black: parallel to the *x*-axis), consistent with temporal change in the HB448 haploblock. The distribution of s is based on simulations of 106 initial and final frequencies of the haploblock that are consistent with the estimated frequencies and error in the estimates. Eq. (S1) was use to calculate a value of s for each set of initial and final frequencies during the time interval between 1883 (early historic) and 2014 (contemporary). The right-hand panel shows the selection coefficients under the balancing selection model that are consistent with observed changes in HB448 inversion frequencies in Europe. Across the range of possible polymorphic equilibrium frequencies under balancing selection, equilibria near unity (*e.g.*, p_{eq} = 0.99) require modestly strong selection (average *S* = 0.032; 95% CI = [0.022, 0.043]) to explain the observed frequency changes in HB448, and lower equilibrium states (*e.g.*, p_{eq} < 0.90) require stronger selection.

974

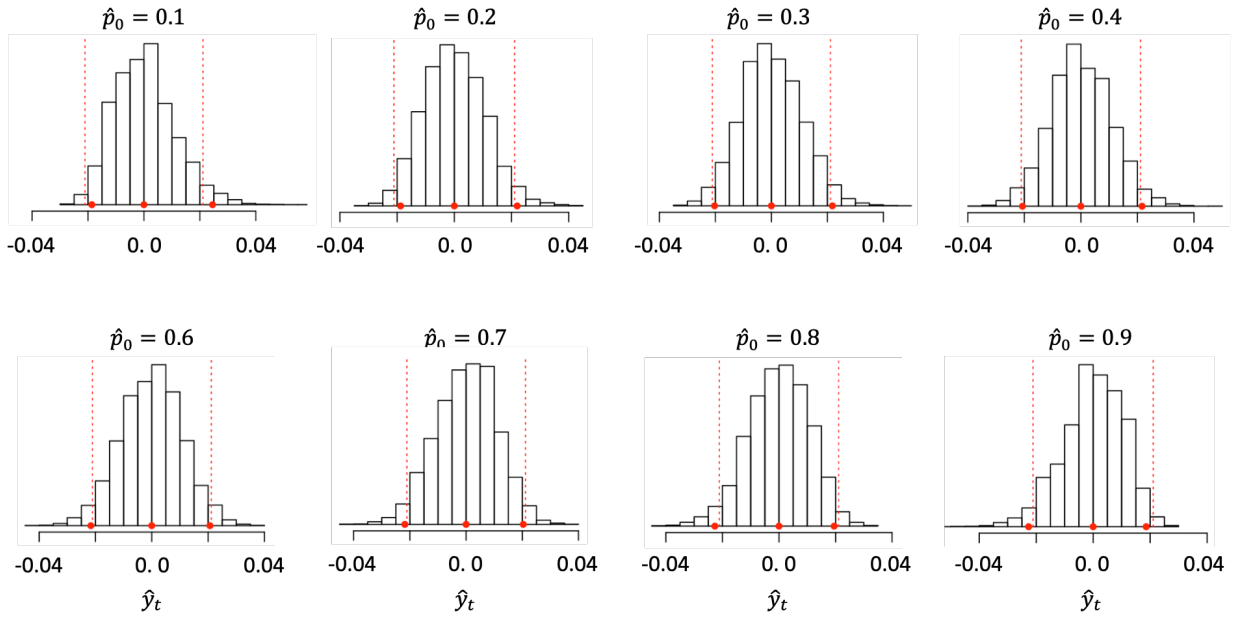

975

976 **Figure S22.** Simulated distribution of the scaled metric of divergence, $\hat{y}_t$, given different estimated
977 values of the initial (historic) allele frequency. Each distribution is based on 10^4 independent and
978 neutrally evolving SNPs. The simulations use n_0 = 182, n_t = 312, and t = 131, with a moderate
979 effective population size (N_e = 10^4). Histograms show the distribution of $\hat{y}_t$ estimates, the red
980 circles show the simulated mean and 95% confidence intervals for simulated data, and the vertical
981 broken red lines show +/- 1.96 SD, where SD is the square root of our analytical expression for
982 $var[\hat{y}_t]$.

SUPPLEMENTARY TEXT

S1: Estimating the strength of selection on HB448 using temporal changes

The putative inversion HB448 increases in frequency between historical and contemporary European populations, consistent with selection favouring its increase in the invasive range. To infer strengths of selection that are sufficient to explain the pattern of frequency change, we considered two simple, deterministic models of selection for the inversion:

- A *positive selection model* in which the inversion is favoured over the standard haplotype and is eventually expected to fix in European populations
- A *balancing selection model* in which the increased frequency of the inversion brings it closer to a hypothetical polymorphic equilibrium within the European range.

We note that, while genetic drift will inevitably play some role in the allele frequency dynamics of loci subject to selection (because populations are finite in size), evolutionary dynamics are well-approximated by deterministic models provided the allele frequencies of favourable variants are at least moderately common in the population and selection is strong relative to the inverse of the effective population size[81]. Both assumptions are easily met for the HB448 haplotype.

Positive selection model

Let p represent the frequency of the HB448 inversion haplotype. Under a model of positive selection with no dominance, the general solution for the ratio of inversion to standard haplotype frequencies (the ratio defined as $x = p/(1 - p)$) is:

$$x_t = x_0(1 + s)^t$$

which is easily rearranged to solve for the frequency of the inversion:

$$p_t = \frac{p_0(1 + s)^t}{1 - p_0 + p_0(1 + s)^t}$$

(*e.g.* [82] pp. 200-203), where s is the fitness increase associated with each copy of the inversion (*i.e.*, the fitnesses of inversion heterozygotes and homozygotes, relative to individuals without the inversion, are $1 + s$ and $(1 + s)^2$, respectively). Under this parameterization, the difference in

relative fitness between inversion and standard haplotype homozygotes is $2s(1 + s/2) \sim 2s$, with the $2s$ approximation applying when s is small (as we infer below).

The strength of selection is a function of the inversion frequency shift from p_0 to p_t following t generations of evolution:

$$s = exp\left[\frac{1}{t} log\left(\frac{p_t(1-p_0)}{p_0(1-p_t)}\right)\right] - 1 \quad (1)$$

Since common ragweed is an annual plant, t refers to the number of years that have transpired, and p_0 and p_t can be estimated (with uncertainty) from the contemporary and historical samples.

We used eq. (1) to infer strengths of selection (s) that would be consistent with the estimated change inversion frequencies over time. We used the estimated inversion frequencies across two time points: (1) 0.4495 in the earlies historical samples with median sampling date of 1883 (n = 109 diploid individuals), and (2) 0.7724 in a contemporary sample from 2014 (n = 156). From these estimates, we simulated 10^6 inversion frequencies per time point, each based on a random sample from the binomial distribution with parameters p and $2n$ corresponding to the estimated frequency and sample size for the relevant time point (the factor of 2 in $2n$ accounts for diploidy).

We used eq. (1) to calculate 10^6 values of s that were compatible with simulated inversion frequencies for time points (1) and (2), and used these to infer the mean and 95% confidence interval for s, given our data.

Balancing selection model

Although temporal changes in the HB448 haplotype are consistent with changes predicted under the positive selection model presented above, we wished to also evaluate an alternative model in which balancing selection favours evolution of the inversion towards an equilibrium polymorphic state. To explore the strength of selection towards a hypothetical equilibrium within the European range, we considered a simple model of overdominant selection. Note that the overdominant selection model is dynamically equivalent to many other balancing selection models provided the differences in fitness among genotypes are small (consistent with our

analysis below). Our results based on the overdominance model should, therefore, apply more broadly to other scenarios of balancing selection, including scenarios involving negative frequency-dependence and antagonistic pleiotropy[83,84].

Following standard theory (*e.g.*, [85] pp. 270-272), the expected change in frequency over a generation (generation t to generation $t + 1$) is:

$$\Delta p_t = p_{t+1} - p_t = \frac{(s_1 + s_2)p_t(1 - p_t)(p_{eq} - p_t)}{1 - p_{eq}(1 - p_{eq})(s_1 + s_2) - (p_t - p_{eq})^2(s_1 + s_2)}$$

where s_1 and s_2 refer to the fitness costs of being homozygous for inversion and standard haplotypes, respectively, and $p_{eq} = s_2(s_1 + s_2)^{-1}$ is the equilibrium frequency of the inversion. Using a continuous-time approximation, we can solve for the overall selection coefficient, $S = s_1 + s_2$, that is consistent with a frequency shift from p_0 to $p_t < p_{eq}$ across t generations:

$$t = \int_{p_0}^{p_t} \frac{1 - Sp_{eq}(1 - p_{eq}) - S(x - p_{eq})^2}{Sx(1 - x)(p_{eq} - x)} dx$$

$$= \frac{\left(p_{eq} - Sp_{eq}(1 - p_{eq})\right) log\left(\frac{1 - p_t}{1 - p_0}\right) + (1 - p_{eq})(1 - Sp_{eq}) log\left(\frac{p_t}{p_0}\right) - \left(1 - Sp_{eq}(1 - p_{eq})\right) log\left(\frac{p_t - p_{eq}}{p_0 - p_{eq}}\right)}{Sp_{eq}(1 - p_{eq})}$$

Solving for S, gives us:

$$S = \frac{p_{eq}\ log\left(\frac{1 - p_t}{1 - p_0}\right) + (1 - p_{eq}) log\left(\frac{p_t}{p_0}\right) - log\left(\frac{p_{eq} - p_t}{p_{eq} - p_0}\right)}{p_{eq}(1 - p_{eq})\left(t + log\left(\frac{1 - p_t}{1 - p_0}\right) + log\left(\frac{p_t}{p_0}\right) - log\left(\frac{p_{eq} - p_t}{p_{eq} - p_0}\right)\right)} \quad (2)$$

To infer the strength of selection (S) that would be consistent with observed inversion frequencies and a given equilibrium value (p_{eq}), we simulated 10^6 inversion frequencies consistent with the estimated frequency and its sample size at historical time point (~1883) and 10^6 frequencies consistent with the estimate for the contemporary sample. (Frequencies were simulated as described in the positive selection model section, above). We used each pair of simulated inversion frequencies and eq. (2) to infer the value of S consistent with the frequency

values. The resulting distribution of 10^6 simulated *S* values was used to calculate 95% CI for *S* consistent with the data. We focused on equilibrium values outside of the 95% CI for contemporary inversion frequencies (*i.e.*, values of p_{eq} between 0.85 and 1). The results show that plausible selection coefficients under scenarios of balancing selection are consistently greater than those of the positive selection model (fig. S21). Selection under the positive selection model can, therefore, be regarded as a lower bound for the strength of selection consistent with the observed temporal changes in European HB448 inversion frequencies.

S2: Selection estimated from spatial changes in haploblock frequency

Cline theory

We will consider the simplest possible population genetics model of local adaptation in a species that is continuously distributed along a single axis of space (*e.g.*, from north to south), with x represent location along the axis, and $x = 0$ representing a point in space where the environment relevant to selection at a focal locus—in this instance, a genomic region segregating for an inversion—changes abruptly. We assume that the inversion is favoured in locations where $x > 0$ (*e.g.*, in the north) and the standard haplotype is favoured in locations where $x < 0$ (*e.g.*, the south). We further assume that population density is uniform across the spatial gradient (at least within the vicinity of the environmental transition), and that individual dispersal follows a symmetric, Gaussian distribution with variance of σ^2 (the unit of distance is arbitrary, though σ and x should have the same units, *e.g.*: if distance in x is measured in kilometres then σ should also be expressed in km; σ^2 corresponds to the migration rate, m, between adjacent patches in discrete stepping stone models)[86].

Given the stated assumptions, the inversion frequency dynamics at location x can be described using the following reaction diffusion equation:

$$\frac{dp(x)}{dt} = \frac{\sigma^2}{2}\frac{d^2p(x)}{dx^2} + \Delta p_{sel}(x)$$

where $\Delta p_{sel}(x)$ is the local response to selection[46,87]. With symmetrical strengths of selection at each side of the environmental transition, and no dominance, then $\Delta p_{sel}(x) \approx sp(x)\big(1 - p(x)\big)$ within the northern region of the range where the inversion is favoured, and $\Delta p_{sel}(x) \approx -sp(x)\big(1 - p(x)\big)$ in the southern portion of the range where the standard haplotype is favoured; both expressions are valid for modest-to-weak selection ($0 < s < \sim 0.1$). As in the positive selection model presented above, this parameterization leads to local fitness differences of ~2s between inversion and standard haplotypes. Incorporating dominance does not change our results provided the dominance relations between the alleles are consistent across the range (*i.e.*, under "parallel dominance"[88]). At equilibrium between selection and migration, the maximum cline slope will be:

$$\left(\frac{dp(x)}{dx}\right) = \sqrt{\frac{s}{3\sigma^2}} \quad (3)$$

Following Roughgarden[87], the equilibrium general solution for the cline is:

$$p(x) = -\frac{1}{2} + \frac{3}{2}\left[tanh\left(x\sqrt{\frac{s}{2\sigma^2}} + \left(\sqrt{\frac{2}{3}}\right)\right)\right]^2 \quad for\ x > 0$$

$$p(x) = \frac{3}{2} - \frac{3}{2}\left[tanh\left(-x\sqrt{\frac{s}{2\sigma^2}} + \left(\sqrt{\frac{2}{3}}\right)\right)\right]^2 \quad for\ x < 0$$

Estimating cline slopes by logistic regression

A logistic regression model for inversion frequency as a function of geographic location (x) is:

$$f(x) = \frac{1}{1 + e^{-(\beta_0 + \beta_1 x)}}$$

The parameters of the model can be estimated by fitting the data to the log-odds (logit):

$$log\left(\frac{f(x)}{1 - f(x)}\right) = \beta_0 + \beta_1 x$$

Using the theoretical cline functions (above) to calculate the log-odds, we obtain the following slopes. For shallow clines—those with a geographically broad clinal region, where the maximum slope can be accurately estimated—we have:

$$\frac{d\ log\left(\frac{p(x)}{1 - p(x)}\right)}{dx} = 4\sqrt{\frac{s}{3\sigma^2}}$$

For steep clines—those with a narrow clinal region, where the maximum slope will be underestimated using the logit function—we have:

$$\frac{d\ log\left(\frac{p(x)}{1-p(x)}\right)}{dx} = \sqrt{\frac{2s}{\sigma^2}}$$

We get the following estimates from these two limits:

$$\frac{\sqrt{3}\beta_1}{4} \leq \frac{\sqrt{s}}{\sigma} \leq \frac{\beta_1}{\sqrt{2}}$$

Given the point estimates and 95% CI for β_1 in table S12, we can calculate plausible ranges for the lower bound of $\frac{\sqrt{s}}{\sigma}$ by multiplying the values for β_1 by $\frac{\sqrt{3}}{4}$

Comparisons of spatially varying selection among haploblocks

All of these estimates rely on the assumption that the system is at equilibrium within each range and time point, though that assumption may be more valid for some cases then others. To the extent that it is a reasonable assumption, and if dispersal (gene flow) is consistent across ranges and times, we can estimate the relative strength of selection in different contexts as:

$$\frac{s_A}{s_B} = \left(\frac{\beta_{1,A}}{\beta_{1,B}}\right)^2$$

where *A* and *B* refer to different ranges or time points.

S3: A simple null model of temporal allele frequency changes under drift

To evaluate whether temporal changes in candidate loci exceeded neutral expectations under drift in the absence of selection, we compared the distribution of the following standardized measure of divergence for a large sample of putatively neutral SNPs with the same metric calculated for selection candidates. Let divergence after *t* generations be defined as:

$$y_t = \frac{p_t - p_0}{\sqrt{t p_0 (1 - p_0)}}$$

where p_0 and p_t represent the initial and final frequencies of an allele at a bi-allelic locus. We shall show below that, provided loci with low minor allele frequencies are first filtered out of the analysis, the metric follows a symmetric distribution that is approximately independent of the initial frequency.

For a locus with initial frequency of p_0, the frequency after one generation of drift is given by:

$$p_1 = \frac{x}{2N_e}$$

where *x* is a random variable drawn from a binomial distribution with parameters $2N_e$ and p_0, where N_e is the effective population size (this follows the standard, Wright-Fisher model of genetic drift). The expected value and the variance for p_1 is therefore p_0 and $p_0(1 - p_0)/2N_e$, respectively. The model can be extrapolated for a modest number of generations, after which the allele frequency (p_t after *t* generations) has an expected value of p_0 and variance of $tp_0(1 - p_0)/2N_e$. The latter will eventually break down as *t* increases, but it should be appropriate provided $t/2N_e$ is small and the initial frequency is not too close to zero or one, as we assume below. From these expressions, the standardized measure of allele frequency divergence in the population under drift (and no selection) has an expectation of zero and a variance of:

$$var(y_t) = \frac{var(p_t)}{t p_0 (1 - p_0)} = \frac{1}{2N_e}$$

which is independent of the initial frequency.

In reality, error in the estimates of p_0 and p_t will also affect the test statistic, and this will tend to inflate the variance, but doesn't alter the conclusion that (under a null model of drift with no selection) the distribution of the estimates of y_t (which we denote as $\hat{y}_t$) will be roughly independent of the initial allele frequencies in the historic sample. If we define $\hat{p}_t$ and $\hat{p}_0$ is the estimates of the allele frequencies, then our test statistic is:

$$\hat{y}_t = \frac{\hat{p}_t - \hat{p}_0}{\sqrt{t\hat{p}_0(1-\hat{p}_0)}}$$

The mean and variance of $\hat{y}_t$ can be calculated using the following steps:

Step 1. The expected value and variance of $\hat{p}_t$ conditioned on the final population frequency (*i.e.*, the true frequency, p_t) is:

$$E[\hat{p}_t|p_t] = p_t$$

$$var[\hat{p}_t|p_t] = \frac{p_t(1-p_t)}{n_t}$$

where n_t represents the number of genes sampled in the contemporary population (*e.g.*, for HB448, 156 individuals were sampled for the contemporary estimate in Europe; given diploidy, we have n_t = 312).

Step 2. The expected value and variance of $\hat{p}_t$ conditioned on the initial population frequency (*i.e.*, the true frequency, p_0) is:

$$E[\hat{p}_t|p_0] = E([\hat{p}_t|p_t]\,|p_0) = E(p_t|p_0) = p_0$$

$$var[\hat{p}_t|p_0] = E(var[\hat{p}_t|p_t]\,|p_0) + var([\hat{p}_t|p_t]\,|p_0) = E\left(\frac{p_t(1-p_t)}{n_t}|p_0\right) + var(p_t|p_0)$$

$$var[\hat{p}_t|p_0] = \frac{E(p_t|p_0)\,(1-E(p_t|p_0)\,) - var(p_t|p_0)}{n_t} + var(p_t|p_0) = \frac{p_0(1-p_0)}{n_t} + \frac{tp_0(1-p_0)}{2N_e}\left(1-\frac{1}{n_t}\right)$$

where N_e is the effective population size, and n_0 is the number of genes sampled in the historic population (*e.g.*, for HB448, 91 individuals were sampled for the contemporary estimate in Europe; given diploidy, we have n_0 = 182).

Step 3. Among loci with an initial frequency estimate of $\hat{p}_0$, the true initial frequency (p_0) will, roughly, follow a distribution with mean and variance of $\hat{p}_0$ and $\hat{p}_0(1-\hat{p}_0)n_0^{-1}$, respectively. Consequently, the expected value and the variance of $\hat{p}_t$ conditioned on the initial frequency estimate $\hat{p}_0$ will be:

$$E[\hat{p}_t|\hat{p}_0] = E\{[\hat{p}_t|p_0]\,|\hat{p}_0\} = E\{p_0|\hat{p}_0\} = \hat{p}_0$$

$$var[\hat{p}_t|\hat{p}_0] = E\{var[\hat{p}_t|p_0]\,|\hat{p}_0\} + var\{E[\hat{p}_t|p_0]\,|\hat{p}_0\} = E\left\{\frac{p_0(1-p_0)}{n_t} + \frac{p_0(1-p_0)}{2N_e}t\left(1-\frac{1}{n_t}\right)|\hat{p}_0\right\} + var\{p_0\,|\hat{p}_0\}$$

$$var[\hat{p}_t|\hat{p}_0] = \hat{p}_0(1-\hat{p}_0)\left[\frac{1}{n_t} + \frac{1}{2N_e}t\left(1-\frac{1}{n_t}\right)\right]\left(1-\frac{1}{n_0}\right) + \frac{\hat{p}_0(1-\hat{p}_0)}{n_0}$$

Therefore, the expected value and the variance for $\hat{y}_t$, given an initial frequency estimate of $\hat{p}_0$, will be:

$$E[\hat{y}_t|\hat{p}_0] = E\left[\frac{\hat{p}_t - \hat{p}_0}{\sqrt{t\hat{p}_0(1-\hat{p}_0)}}|\hat{p}_0\right] = 0$$

$$var[\hat{y}_t|\hat{p}_0] = \frac{var[\hat{p}_t|\hat{p}_0]}{t\hat{p}_0(1-\hat{p}_0)} = \frac{\left[\frac{1}{n_t} + \frac{1}{2N_e}t\left(1-\frac{1}{n_t}\right)\right]\left(1-\frac{1}{n_0}\right) + \frac{1}{n_0}}{t}$$

Note that the final expressions are, once again, independent of the initial frequency, though (once again) the pathway to these results requires that $\hat{p}_0$ is not too close to zero or one. Because of this independence, we can pool loci with different initial frequency estimates (with pooling after loci with low minor allele frequency are first removed) to approximate the null distribution for $\hat{y}_t$ as well as the variance of the test statistic: $var[\hat{y}_t] = var[\hat{y}_t|\hat{p}_0]$.

Incidentally, the expression for $var[\hat{y}_t|\hat{p}_0]$ can be rearranged by solving for the effective population size across the *t* generations, *i.e.*:

1245
$$N_e = \frac{\frac{1}{2}t\left(1-\frac{1}{n_t}\right)\left(1-\frac{1}{n_0}\right)}{tvar[\hat{y}_t] \; -\frac{1}{n_0}-\frac{1}{n_t}\left(1-\frac{1}{n_0}\right)}$$

1246

1247 A rough estimate of N_e can be obtained from a set of independent neutral SNPs by using the
1248 above formula with the estimated variance of $\hat{y}_t$ substituted for $var[\hat{y}_t]$.

1249

1250 *Simulations*

1251 We carried simulations to test the theoretical predictions of the neutral model presented above,
1252 and find that they work well as long as initial allele frequency estimates are not too close to zero
1253 or one ($0.1 < \hat{p}_0 < 0.9$ performs well and $0.2 < \hat{p}_0 < 0.8$ is excellent). Simulations for a given
1254 value of $\hat{p}_0$ were carried out using the following steps. First, we used rejection sampling to
1255 simulate a distribution of initial population frequencies (p_0) for a given value of $\hat{p}_0$. For each
1256 SNP, we sampled a true population frequency (p_0) from a neutral stationary distribution (*i.e.*, a
1257 single draw from a symmetric beta distribution with parameters theta = 0.05, which corresponds
1258 to the population-scaled mutation rate for the locus)[89]. We then generated a frequency estimate
1259 for the SNP from a single draw from a binomial distribution with parameters p_0 and n_0 = 182,
1260 where n_0 is the number of genes sampled in the historic population. We retained the first 10^4
1261 simulated SNPs whose estimate after binomial sampling matched the focal value of $\hat{p}_0$. From
1262 the retained SNPs, we carried out forward Wright-Fisher simulations under pure drift for *t*
1263 generations to determine the contemporary population frequency (p_t) for each SNP. We then
1264 carried out a second round of binomial sampling (with parameters p_t and n_t) for each SNP to
1265 generate a final allele frequency estimate. The frequency estimates were used to calculate $\hat{y}_t$
1266 for each simulated SNP. Fig. S22 shows simulated distributions of $\hat{y}_t$ for different values initial
1267 frequency estimates ($\hat{p}_0$). The distributions are roughly independent of $\hat{p}_0$ and their 95% CI are
1268 well-approximated by the 95% confidence interval predicted by a normal distribution with
1269 variance corresponding to our analytical expression for $var[\hat{y}_t]$ (see above).

REFERENCES

1. Colautti, R. I., Maron, J. L. & Barrett, S. C. H. Common garden comparisons of native and introduced plant populations: latitudinal clines can obscure evolutionary inferences. *Evol. Appl.* **2**, 187–199 (2009).
2. Oduor, A. M. O., Leimu, R. & van Kleunen, M. Invasive plant species are locally adapted just as frequently and at least as strongly as native plant species. *J. Ecol.* **104**, 957–968 (2016).
3. Hodgins, K. A., Bock, D. G. & Rieseberg, L. H. Trait evolution in invasive species. *Annual Plant Reviews Online* 459–496 (2018).
4. Colautti, R. I. & Barrett, S. C. H. Rapid adaptation to climate facilitates range expansion of an invasive plant. *Science* **342**, 364–366 (2013).
5. Essl, F. *et al.* Biological flora of the British isles:Ambrosia artemisiifolia. *J. Ecol.* **103**, 1069–1098 (2015).
6. Bagarozzi, D. A., Jr & Travis, J. Ragweed pollen proteolytic enzymes: possible roles in allergies and asthma. *Phytochemistry* **47**, 593–598 (1998).
7. Schaffner, U. *et al.* Biological weed control to relieve millions from Ambrosia allergies in Europe. *Nat. Commun.* **11**, 1745 (2020).
8. Lake, I. R. *et al.* Climate Change and Future Pollen Allergy in Europe. *Environ. Health Perspect.* **125**, 385–391 (2017).
9. Ziska, L. *et al.* Recent warming by latitude associated with increased length of ragweed pollen season in central North America. *Proc. Natl. Acad. Sci. U. S. A.* **108**, 4248–4251 (2011).
10. van Boheemen, L. A. & Hodgins, K. A. Rapid repeatable phenotypic and genomic adaptation following multiple introductions. *Mol. Ecol.* **29**, 4102–4117 (2020).
11. Bieker, V. C. *et al.* Uncovering the hologenomic basis of an extraordinary plant invasion. *bioRxiv* (2022) doi:10.1101/2022.02.03.478494.

12. Chauvel, B., Dessaint, F., Cardinal-Legrand, C. & Bretagnolle, F. The historical spread of Ambrosia artemisiifolia L. in France from herbarium records. *J. Biogeogr.* **33**, 665–673 (2006).
13. van Boheemen, L. A. *et al.* Multiple introductions, admixture and bridgehead invasion characterize the introduction history of Ambrosia artemisiifolia in Europe and Australia. *Mol. Ecol.* **26**, 5421–5434 (2017).
14. van Boheemen, L. A., Atwater, D. Z. & Hodgins, K. A. Rapid and repeated local adaptation to climate in an invasive plant. *New Phytol.* **222**, 614–627 (2019).
15. Seebens, H. *et al.* No saturation in the accumulation of alien species worldwide. *Nat. Commun.* **8**, 14435 (2017).
16. Fisher, R. A. *The Genetical Theory of Natural Selection*. (The Clarendon Press, 1930).
17. Kimura, M. *The Neutral Theory of Molecular Evolution*. (Cambridge University Press, 1983).
18. Orr, H. A. The population genetics of adaptation: The distribution of factors fixed during adaptive evolution. *Evolution* **52**, 935–949 (1998).
19. Yeaman, S. & Whitlock, M. C. The genetic architecture of adaptation under migration-selection balance. *Evolution* **65**, 1897–1911 (2011).
20. Yeaman, S., Gerstein, A. C., Hodgins, K. A. & Whitlock, M. C. Quantifying how constraints limit the diversity of viable routes to adaptation. *PLoS Genet.* **14**, e1007717 (2018).
21. Hermisson, J. & Pennings, P. S. Soft sweeps: molecular population genetics of adaptation from standing genetic variation. *Genetics* **169**, 2335–2352 (2005).
22. Kirkpatrick, M. & Barton, N. Chromosome inversions, local adaptation and speciation. *Genetics* **173**, 419–434 (2006).
23. Wellenreuther, M. & Bernatchez, L. Eco-Evolutionary Genomics of Chromosomal Inversions. *Trends Ecol. Evol.* **33**, 427–440 (2018).
24. Krimbas, C. B. & Powell, J. R. *Drosophila Inversion Polymorphism*. (CRC Press, 1992).
25. Lowry, D. B. & Willis, J. H. A widespread chromosomal inversion polymorphism contributes

to a major life-history transition, local adaptation, and reproductive isolation. *PLoS Biol.* **8**, (2010).

26. Todesco, M. *et al.* Massive haplotypes underlie ecotypic differentiation in sunflowers. *Nature* **584**, 602–607 (2020).
27. Kirkpatrick, M. & Barrett, B. Chromosome inversions, adaptive cassettes and the evolution of species' ranges. *Mol. Ecol.* **24**, 2046–2055 (2015).
28. Guan, D. *et al.* Identifying and removing haplotypic duplication in primary genome assemblies. *Bioinformatics* **36**, 2896–2898 (2020).
29. Putnam, N. H. *et al.* Chromosome-scale shotgun assembly using an in vitro method for long-range linkage. *Genome Res.* **26**, 342–350 (2016).
30. Payne, W. W., Raven, P. H. & Kyhos, D. W. Chromosome numbers in compositae. Iv. Ambrosieae. *Am. J. Bot.* **51**, 419–424 (1964).
31. Kubešová, M. *et al.* Naturalized plants have smaller genomes than their non-invading relatives: a flow cytometric analysis of the Czech alien flora. *Preslia* **82**, 81–96 (2010).
32. Bai, C., Alverson, W. S., Follansbee, A. & Waller, D. M. New reports of nuclear DNA content for 407 vascular plant taxa from the United States. *Ann. Bot.* **110**, 1623–1629 (2012).
33. Manni, M., Berkeley, M. R., Seppey, M., Simão, F. A. & Zdobnov, E. M. BUSCO Update: Novel and Streamlined Workflows along with Broader and Deeper Phylogenetic Coverage for Scoring of Eukaryotic, Prokaryotic, and Viral Genomes. *Mol. Biol. Evol.* **38**, 4647–4654 (2021).
34. Barker, M. S. *et al.* Multiple paleopolyploidizations during the evolution of the Compositae reveal parallel patterns of duplicate gene retention after millions of years. *Mol. Biol. Evol.* **25**, 2445–2455 (2008).
35. Badouin, H. *et al.* The sunflower genome provides insights into oil metabolism, flowering and Asterid evolution. *Nature* **546**, 148–152 (2017).

36. Holt, C. & Yandell, M. MAKER2: an annotation pipeline and genome-database management tool for second-generation genome projects. *BMC Bioinformatics* **12**, 491 (2011).

37. Zagotta, M. T. *et al.* The Arabidopsis ELF3 gene regulates vegetative photomorphogenesis and the photoperiodic induction of flowering. *Plant J.* **10**, 691–702 (1996).

38. Martin, A. & Orgogozo, V. The Loci of repeated evolution: a catalog of genetic hotspots of phenotypic variation. *Evolution* **67**, 1235–1250 (2013).

39. Gautier, M. Genome-Wide Scan for Adaptive Divergence and Association with Population-Specific Covariates. *Genetics* **201**, 1555–1579 (2015).

40. Fick, S. E. & Hijmans, R. J. WorldClim 2: new 1-km spatial resolution climate surfaces for global land areas. *Int. J. Climatol.* **37**, 4302–4315 (2017).

41. Booker, T. R., Yeaman, S. & Whitlock, M. C. The WZA: A window-based method for characterizing genotype-environment association. *bioRxiv* 2021.06.25.449972 (2021) doi:10.1101/2021.06.25.449972.

42. Prapas, D. *et al.* QTL analysis reveals an oligogenic architecture of a rapidly adapting trait during the European invasion of common ragweed. *bioRxiv* (2022) doi:10.1101/2022.02.24.481758.

43. Werck-Reichhart, D., Bak, S. & Paquette, S. Cytochromes p450. *Arabidopsis Book* **1**, e0028 (2002).

44. Gupta, R. & Chakrabarty, S. K. Gibberellic acid in plant: still a mystery unresolved. *Plant Signal. Behav.* **8**, (2013).

45. Li, H. & Ralph, P. Local PCA Shows How the Effect of Population Structure Differs Along the Genome. *Genetics* **211**, 289–304 (2019).

46. Haldane, J. B. S. The theory of a cline. *J. Genet.* **48**, 277–284 (1948).

47. Thurman, T. J. & Barrett, R. D. H. The genetic consequences of selection in natural populations. *Mol. Ecol.* **25**, 1429–1448 (2016).

1374 48. Chen, K.-W., Marusciac, L., Tamas, P. T., Valenta, R. & Panaitescu, C. Ragweed Pollen
1375 Allergy: Burden, Characteristics, and Management of an Imported Allergen Source in
1376 Europe. *Int. Arch. Allergy Immunol.* **176**, 163–180 (2018).
1377 49. Stern, D. L. The genetic causes of convergent evolution. *Nat. Rev. Genet.* **14**, 751–764
1378 (2013).
1379 50. Sun, Y. *et al.* Climate warming can reduce biocontrol efficacy and promote plant invasion
1380 due to both genetic and transient metabolomic changes. *Ecol. Lett.* **25**, 1387–1400 (2022).
1381 51. Cheng, H., Concepcion, G. T., Feng, X., Zhang, H. & Li, H. Haplotype-resolved de novo
1382 assembly using phased assembly graphs with hifiasm. *Nat. Methods* **18**, 170–175 (2021).
1383 52. Marçais, G. & Kingsford, C. A fast, lock-free approach for efficient parallel counting of
1384 occurrences of k-mers. *Bioinformatics* **27**, 764–770 (2011).
1385 53. Li, H. Aligning sequence reads, clone sequences and assembly contigs with BWA-MEM.
1386 *arXiv [q-bio.GN]* (2013).
1387 54. Sayers, E. W. *et al.* Database resources of the National Center for Biotechnology
1388 Information. *Nucleic Acids Res.* **49**, D10–D17 (2021).
1389 55. Schubert, M., Lindgreen, S. & Orlando, L. AdapterRemoval v2: rapid adapter trimming,
1390 identification, and read merging. *BMC Res. Notes* **9**, 88 (2016).
1391 56. Schubert, M. *et al.* Characterization of ancient and modern genomes by SNP detection and
1392 phylogenomic and metagenomic analysis using PALEOMIX. *Nat. Protoc.* **9**, 1056–1082
1393 (2014).
1394 57. Van der Auwera, G. A. & O'Connor, B. D. *Genomics in the Cloud: Using Docker, GATK,*
1395 *and WDL in Terra*. ('O'Reilly Media, Inc.', 2020).
1396 58. DePristo, M. A. *et al.* A framework for variation discovery and genotyping using next-
1397 generation DNA sequencing data. *Nat. Genet.* **43**, 491–498 (2011).
1398 59. Danecek, P. *et al.* The variant call format and VCFtools. *Bioinformatics* **27**, 2156–2158
1399 (2011).

1400 60. Browning, B. L., Zhou, Y. & Browning, S. R. A One-Penny Imputed Genome from Next-
1401 Generation Reference Panels. *The American Journal of Human Genetics* vol. 103 338–348
1402 (2018).
1403 61. Flynn, J. M. *et al.* RepeatModeler2 for automated genomic discovery of transposable
1404 element families. *Proc. Natl. Acad. Sci. U. S. A.* **117**, 9451–9457 (2020).
1405 62. Campbell, M. S. *et al.* MAKER-P: a tool kit for the rapid creation, management, and quality
1406 control of plant genome annotations. *Plant Physiol.* **164**, 513–524 (2014).
1407 63. Smit, A. F. A., Hubley, R. & Green, P. RepeatMasker Open-4.0. 2013--2015. (2015).
1408 64. Acids research, N. & 2021. UniProt: the universal protein knowledgebase in 2021. *Nucleic*
1409 *Acids Res.* **49**, D480–D489 (2021).
1410 65. Parra, G., Bradnam, K. & Korf, I. CEGMA: a pipeline to accurately annotate core genes in
1411 eukaryotic genomes. *Bioinformatics* **23**, 1061–1067 (2007).
1412 66. Korf, I. Gene finding in novel genomes. *BMC Bioinformatics* **5**, 59 (2004).
1413 67. Berardini, T. Z. *et al.* The arabidopsis information resource: Making and mining the 'gold
1414 standard' annotated reference plant genome. *genesis* vol. 53 474–485 (2015).
1415 68. Camacho, C. *et al.* BLAST+: architecture and applications. *BMC Bioinformatics* **10**, 421
1416 (2009).
1417 69. Alexa, A. & Rahnenführer, J. Gene set enrichment analysis with topGO. *Bioconductor*
1418 *Improv* **27**, 1–26 (2009).
1419 70. Bouché, F., Lobet, G., Tocquin, P. & Périlleux, C. FLOR-ID: an interactive database of
1420 flowering-time gene networks in Arabidopsis thaliana. *Nucleic Acids Res.* **44**, D1167–71
1421 (2016).
1422 71. Cingolani, P. *et al.* A program for annotating and predicting the effects of single nucleotide
1423 polymorphisms, SnpEff: SNPs in the genome of Drosophila melanogaster strain w1118;
1424 iso-2; iso-3. **6**, 80–92 (2012).
1425 72. Chang, C. C. *et al.* Second-generation PLINK: rising to the challenge of larger and richer

datasets. *GigaScience* vol. 4 (2015).

73. Hijmans, R. J. *et al.* Package 'raster'. *R package* **734**, (2015).
74. Team, R. C. & Others. R: A language and environment for statistical computing. (2013).
75. Kang, H. M. *et al.* Variance component model to account for sample structure in genome-wide association studies. *Nat. Genet.* **42**, 348–354 (2010).
76. Fox, J. *et al.* The car package. *R Foundation for Statistical Computing* **1109**, (2007).
77. Korneliussen, T. S., Albrechtsen, A. & Nielsen, R. ANGSD: Analysis of Next Generation Sequencing Data. *BMC Bioinformatics* **15**, 356 (2014).
78. Meisner, J. & Albrechtsen, A. Inferring Population Structure and Admixture Proportions in Low-Depth NGS Data. *Genetics* **210**, 719–731 (2018).
79. Lenth, R., Singmann, H., Love, J., Buerkner, P. & Herve, M. Package 'emmeans'. (2019).
80. Rastas, P., Paulin, L., Hanski, I., Lehtonen, R. & Auvinen, P. Lep-MAP: fast and accurate linkage map construction for large SNP datasets. *Bioinformatics* **29**, 3128–3134 (2013).
81. Otto, S. P. & Day, T. *A Biologist's Guide to Mathematical Modeling in Ecology and Evolution*. (Princeton University Press, 2011).
82. Hartl, D. L. & Clark, A. G. *Principles of Population Genetics*. (Sinauer, 2007).
83. Connallon, T. & Clark, A. G. Antagonistic versus nonantagonistic models of balancing selection: characterizing the relative timescales and hitchhiking effects of partial selective sweeps. *Evolution* **67**, 908–917 (2013).
84. Chevin, L., Gompert, Z. & Nosil, P. Frequency dependence and the predictability of evolution in a changing environment. *Evolution Letters* vol. 6 21–33 (2022).
85. Crow, J. F. & Kimura, M. *An Introduction to Population Genetics Theory*. vol. 26 977 (The Blackburn Press, 1971).
86. Felsenstein, J. *Theoretical Evolutionary Genetics*. (2019).
87. Roughgarden, J. *Theory of population genetics and evolutionary ecology: an introduction*. (sidalc.net, 1979).

1452 88. Lasne, C., Sgrò, C. M. & Connallon, T. The Relative Contributions of the X Chromosome
1453 and Autosomes to Local Adaptation. *Genetics* **205**, 1285–1304 (2017).
1454 89. Wright, S. Evolution in Mendelian Populations. *Genetics* **16**, 97–159 (1931).